



The MAVERIC Survey: Chandra/ACIS Catalog of Faint X-Ray Sources in 38 Galactic Globular Clusters

Arash Bahramian¹, Jay Strader², James C. A. Miller-Jones¹, Laura Chomiuk², Craig O. Heinke³, Thomas J. Maccarone⁴, David Pooley⁵, Laura Shishkovsky², Vlad Tudor¹, Yue Zhao³, Kwan Lok Li⁶, Gregory R. Sivakoff³, Evangelia Tremou⁷, and Johannes Buchner⁸

¹ International Centre for Radio Astronomy Research-Curtin University, GPO Box U1987, Perth, WA 6845, Australia; arash.bahramian@curtin.edu.au

² Center for Data Intensive and Time Domain Astronomy, Department of Physics and Astronomy, Michigan State University, East Lansing, Michigan 48824, USA

³ Physics Department, University of Alberta, 4-183 CCIS, Edmonton, AB T6G 2E1, Canada

⁴ Department of Physics and Astronomy, Texas Tech University, Box 41051, Lubbock, TX 79409-1051, USA

⁵ Department of Physics and Astronomy, Trinity University, San Antonio, TX, USA

⁶ Institute of Astronomy, National Tsing Hua University, Hsinchu 30013, Taiwan

⁷ LESIA, Observatoire de Paris, CNRS, PSL, SU/UPD, Meudon, France

⁸ Max-Planck-Institut für Extraterrestrische Physik, Gießenbachstraße 1, D-85748 Garching, Germany

Received 2020 May 1; revised 2020 July 7; accepted 2020 July 8; published 2020 September 21

Abstract

Globular clusters host a variety of lower-luminosity ($L_X < 10^{35}$ erg s⁻¹) X-ray sources, including accreting neutron stars (NSs) and black holes (BHs), millisecond pulsars (MSPs), cataclysmic variables, and chromospherically active binaries. In this paper, we provide a comprehensive catalog of more than 1100 X-ray sources in 38 Galactic globular clusters (GCs) observed by the Chandra X-ray Observatory’s Chandra/ACIS detector. The targets are selected to complement the MAVERIC survey’s deep radio continuum maps of Galactic GCs. We perform photometry and spectral analysis for each source, determine a best-fit model, and assess the possibility of it being a foreground or background source based on its spectral properties and location in the cluster. We also provide basic assessments of variability. We discuss the distribution of X-ray binaries in GCs and their X-ray luminosity function, and we carefully analyze systems with $L_X > 10^{33}$ erg s⁻¹. Among these moderately bright systems, we discover a new source in NGC 6539 that may be a candidate accreting stellar-mass BH or a transitional MSP. We show that quiescent NS low-mass X-ray binaries in GCs may spend $\sim 2\%$ of their lifetimes as transitional MSPs in their active ($L_X > 10^{33}$ erg s⁻¹) state. Finally, we identify a substantial underabundance of bright ($L_X > 10^{33}$ erg s⁻¹) intermediate polars in GCs compared to the Galactic field, in contrast with the literature of the past two decades.

Unified Astronomy Thesaurus concepts: Globular star clusters (656); Low-mass x-ray binary stars (939); Neutron stars (1108); Astrophysical black holes (98); Stellar accretion disks (1579); Celestial objects catalogs (212)

Supporting material: figure set, machine-readable table

1. Introduction

An X-ray binary (XRB) is a system where a compact object (white dwarf (WD), neutron star (NS), or black hole (BH)) is accreting from a companion star. The companion is typically a main-sequence star, but it can also be an evolved star or a WD. Observations have shown that XRBs are significantly overabundant in globular clusters (GCs) compared to the field (both in the Milky Way and other galaxies; Clark 1975; Sarazin et al. 2003; Kundu et al. 2007; Kundu & Zepf 2007). This overabundance has been linked to dynamical XRB formation channels in GCs. In the field, these systems form through binary evolution. In GCs, many are formed through stellar interactions made possible by the high population density in GCs. These channels include interaction of a red giant with a compact object (Sutantyo 1975), tidal capture of a companion by the compact object (Fabian et al. 1975), or an exchange interaction, where a compact object replaces a low-mass star in a binary (Hills 1976).

These formation channels rely strongly on encounters in dense environments, and thus they are expected to correlate with some

properties of GCs. One cluster property that influences the frequency of encounters—and thus the production of XRBs—is the “stellar encounter rate,” generally written as $\Gamma \propto \int \frac{\rho^2}{\sigma} dV$, integrated over the GC volume, where ρ is the cluster density and σ is the cluster velocity dispersion (Verbunt & Hut 1987). A strong correlation between the population of XRBs and stellar encounter rate has been observed in Galactic GCs (Pooley et al. 2003; Heinke et al. 2003b; Bahramian et al. 2013), confirming that XRBs are formed through encounters in dense clusters. Dynamical interactions can also destroy primordial binaries (e.g., Davies 1997), and this process can dominate over dynamical formation in lower-density GCs (Heinke et al. 2020).

X-ray sources in GCs consist of multiple subpopulations. These include XRBs like cataclysmic variables (CVs; where a WD accretes from a low-mass star), low-mass X-ray binaries (LMXBs) with a BH or NS accreting from a low-mass ($\lesssim M_\odot$) star, and millisecond pulsars (MSPs), which are thought to be descendants of NS-LMXBs. Furthermore, there is also a small group of bright, chromospherically active binaries (ABs), which contain two tidally locked main-sequence stars in close orbit. The tidally locked orbit in these systems allows their combined X-ray luminosity to reach $\gtrsim 10^{30}$ erg s⁻¹, likely through an enhanced dynamo resulting from the increased rotational velocities (e.g., Walter & Bowyer 1981). While ABs are abundant in GCs and form a large fraction of sources with

$\lesssim 10^{31}$ erg s⁻¹, only a small fraction of them reach $\gtrsim 10^{31}$ erg s⁻¹. It has been demonstrated that fainter X-ray sources in GCs (which are mostly ABs) are likely primordial in origin as their numbers appear correlated with GC mass (Bassa et al. 2004, 2008; Cheng et al. 2018; Heinke et al. 2020).

It is difficult to confidently determine the nature of a faint XRB in a GC based on X-rays alone, and objects thought to be confidently classified primarily from X-rays later turn out to have been typed incorrectly (e.g., Miller-Jones et al. 2015). Adding in observations from additional wavelengths has helped in classifying numerous X-ray sources in various Galactic GCs (e.g., Grindlay et al. 2001; Pooley et al. 2002; Edmonds et al. 2003; Heinke et al. 2006b; Lugger et al. 2007; Maxwell et al. 2012). Still, the nature of many GC X-ray sources remains elusive.

CVs are the most abundant group of XRBs in GCs (e.g., Grindlay et al. 2001; Pooley et al. 2002; Cohn et al. 2010; Lugger et al. 2017; Rivera Sandoval et al. 2018a). CVs in GCs can be formed primordially (via binary formation and evolution) or through dynamical interactions (Davies 1997; Ivanova et al. 2006; Shara & Hurley 2006; Hong et al. 2017; Belloni et al. 2019). However, most present-day CVs in GCs appear to be formed dynamically (Ivanova et al. 2006), and it has been suggested that most of the primordial CVs have been disrupted (at least in some GCs; Davies 1997).

Almost all bright ($L_X > 10^{34}$ erg s⁻¹) XRBs in Galactic GCs have been proven to be NS-LMXBs⁹ (e.g., Bahramian et al. 2014), either through detection of pulsations or X-ray bursts. Additionally, numerous faint ($L_X < 10^{34}$ erg s⁻¹) X-ray sources in Galactic GCs have been identified as quiescent NS-LMXBs, typically through the detection of a thermal component consistent with an NS (e.g., Grindlay et al. 2001; Rutledge et al. 2002; Pooley et al. 2002; Heinke et al. 2003a, 2005b; Servillat et al. 2008; Guillot et al. 2009; Maxwell et al. 2012). The quiescent NS-LMXBs in GCs (with low reddening) provide some of the best samples to study properties of NSs like low-level accretion, crustal cooling, and constraints on mass and radius of NSs (Degenaar et al. 2011; Bahramian et al. 2015; Rivera Sandoval et al. 2018b; Ootes et al. 2019; Guillot et al. 2013; Steiner et al. 2018).

GCs harbor a large population of radio MSPs (Ransom et al. 2005; Hessels et al. 2007; Freire et al. 2017; Dai et al. 2020), some of which have been detected in X-rays (e.g., Bhattacharya et al. 2017; Bogdanov et al. 2010). MSPs are the “recycled” descendants of NS-LMXBs. This link was first proposed upon discovery of the first rotation-powered MSP (Alpar et al. 1982), and the observation of accreting millisecond X-ray pulsars provided strong indirect evidence in support of it (Wijnands & van der Klis 1998). It was strengthened further by the discovery of transitional MSPs (tMSPs), which are NS-LMXBs that switch between rotation-powered radio pulsations and accretion-powered X-ray pulsations (Archibald et al. 2009; de Martino et al. 2010, 2013; Papitto et al. 2013; Bassa et al. 2014; Linares 2014). Today, there are >150 MSPs identified from radio observations of GCs¹⁰ showing a link between dynamical formation and their population (Bagchi et al. 2011; Hui et al. 2011; Bahramian et al. 2013). Additionally, while there are still very few tMSPs known to date, at least two (one confirmed and one candidate) are located in GCs, hinting at a possible overabundance of tMSPs in GCs (IGR J18245–2452 in M28

and Terzan 5 CX1 in Terzan 5; Papitto et al. 2013; Bahramian et al. 2018).

The presence of BHs in GCs has been heavily debated over the past few decades. While initial stellar evolution in GCs is expected to have produced a high number of BHs, there are very few confirmed in them so far. Theoretical studies once favored the contention that all (or almost all) BHs would mass-segregate to the cluster core and get kicked out of GCs rather quickly (Sigurdsson & Hernquist 1993). This contention appears to be consistent with observational studies of bright ($L_X > 10^{35}$ erg s⁻¹) XRBs in GCs, which showed that all of these systems are NS-LMXBs (Verbunt & Lewin 2006; Papitto et al. 2013; Bahramian et al. 2014). This strengthened theories that perhaps *all* BHs get kicked out of GCs (Kulkarni et al. 1993). In recent years, the detection of accreting BH candidates in Galactic and extragalactic GCs (e.g., Maccarone et al. 2007; Strader et al. 2012; Chomiuk et al. 2013; Miller-Jones et al. 2015; Shishkovsky et al. 2018) and the discovery of dynamically confirmed detached BHs in wide-orbit binaries in the Galactic GC NGC 3201 (Giesers et al. 2018, 2019) reversed these earlier suggestions and indicated that a subset of BHs do indeed survive in GCs. A parallel revolution in theoretical work now suggests that many BHs are likely to be retained in GCs (e.g., Morscher et al. 2013, 2015) and perhaps even form BH–BH binaries that merge and can be detected by gravitational wave observatories (Rodriguez et al. 2016).

Determining the nature of the compact object in LMXBs is challenging. In bright outbursting or persistent systems, the detection of pulsations or X-ray bursts indicates an NS accretor, but the absence of these signatures does not reject it. The problem becomes more difficult in quiescent systems where these signatures are challenging or impossible to detect. For some binaries, components in the X-ray spectrum, like a soft blackbody-like emission from the surface of the NS in NS-LMXBs, can help determine the nature of the source (e.g., Rutledge et al. 2002). Another method, which has come into vogue in the last decade, is based on the coupling between the accretion flow and the possible presence of a radio jet: while both BHs and NSs show evidence for jets, BHs tend to be brighter in the radio than NSs by a factor of ~ 5 to 20 (at least at some X-ray luminosities; Fender et al. 2003; Migliari & Fender 2006; Tudor et al. 2017; Gallo et al. 2018).

The MAVERIC survey is focused on identifying accreting BH candidates and other exotic binaries in a large sample of Galactic GCs through radio observations with the Karl G. Jansky Very Large Array (VLA) and the Australia Telescope Compact Array (ATCA; Shishkovsky et al. 2018; Tremou et al. 2018). The goal of the present work is to produce a catalog of X-ray sources in all Galactic GCs without existing comprehensive X-ray studies to accompany the MAVERIC radio continuum data.

In this paper, we provide a full catalog of faint X-ray sources in 38 Galactic GCs based on analysis of available Chandra/ACIS observations. In Section 2, we present sample selection, data, and reduction; in Section 3, we provide details of our analysis method; and in Section 4, we present the source catalog and discuss various measured and estimated source properties in the catalog. Finally, in Section 5, we discuss the impact of this catalog on our understanding of the XRB population in GCs and the nature of the brightest sources in this catalog, including a new BH-LMXB candidate. This study, along with the MAVERIC survey (L. Shishkovsky et al. 2020,

⁹ https://bersavosh.github.io/research/gc_lmxbs.html

¹⁰ See P. Freire’s catalog: <http://naic.edu/~pfreire/GCpsr.html>.

in preparation; V. Tudor et al. 2020, in preparation), will enable a careful multiwavelength study of accreting systems in Galactic GCs.

2. Data and Reduction

2.1. Sample Selection

The MAVERIC sample was initially chosen as all Galactic GCs within 9 kpc and $>10^5 M_{\odot}$, plus a few more massive GCs at larger distances, for a total sample of 50 GCs. The present catalog only includes GCs that have been observed by Chandra/ACIS at least once and that have no X-ray sources in outburst within the cluster. This selection ensures the presence of spectral information from Chandra/ACIS (as opposed to Chandra/HRC, which lacks sufficient spectral resolution for our purposes).

The extended tail of the point-spread function (PSF) for bright ($F_X \gg 10^{-12} \text{ erg s}^{-1} \text{ cm}^{-2}$) X-ray sources severely impacts the detection threshold and completeness for nearby faint sources in Chandra/ACIS observations. Thus, some GCs are excluded because of persistent bright XRBs (M15, NGC 6441, NGC 6624, NGC 6652, NGC 6712), while others (Liller 1, Terzan 6) had Chandra observations only taken during bright outbursts.

We also excluded Omega Cen, 47 Tuc, and NGC 6752 as deep X-ray source catalogs on these clusters have been recently published (Forestell et al. 2014; Bhattacharya et al. 2017; Henleywillis et al. 2018; Cheng et al. 2019b).

These criteria provide us with a sample of 38 GCs (Table 1). Of these 38, 10 have new data taken as part of MAVERIC: six (Djorg 2, M10, M19, NGC 4372, NGC 4833, and M107) have single Chandra/ACIS observations obtained specifically for MAVERIC follow-up, while four others (M22, M62, Terzan 1, and Terzan 5) have both previous data and newer MAVERIC follow-up data.

2.2. Data Reduction

We used CIAO 4.8 and higher (as there were software updates over the duration of the project), with CalDB 4.7.7 and higher for all Chandra data reduction¹¹ (Fruscione et al. 2006), and extracted data products and performed the analysis using ACIS-EXTRACT (hereafter AE; Broos et al. 2010) and the Bayesian X-ray analysis package BXA (Buchner et al. 2014). Our overall goal was to obtain a carefully vetted, consistently analyzed X-ray source catalog for the GCs in our sample. Thus, we first reprocessed the data and produced input files necessary for a high-level analysis (event files, exposure maps, aspect solutions, source catalogs, and so on) using CIAO and used these as input (after inspection and modification, where necessary) for analysis in AE. Finally, we used the spectra produced by AE for spectral analysis in BXA (Section 3). We checked all observations for background flares. We found noticeable flares in four observations out of 90 analyzed in this work. Out of these four, three are negligible because of their short duration compared to the full observation and weak amplitude (Obs. IDs 2683, 3798, and 18997 in M28, Terzan 5, and M30, respectively). However, flaring in one observation (Obs. ID 5435 in NGC 6544) is strong (increasing the background by a factor of ~ 8) and lasts for 5 ks. Thus for

the case of Obs. ID 5435, we followed the standard procedure to remove background flares.¹²

Given the large amount of data, we partially automated the data reduction process using the module `ciao_contrib.runtool` in PYTHON, provided in the CIAO package. All observations were first reprocessed using `chandra_repro`, then we produced exposure maps and image files using the task `fluximage` in the 0.5–10 keV band, with an image binning factor of 0.5. A small (<1) binning factor can improve detection of faint sources in crowded regions (like the core of some GCs) on the Chandra/ACIS detector.

In many observations covering the GCs in our sample, the fields of view (FOV) covered are substantially larger than the half-light radius of the target GC. As we are only interested in sources within the GCs, we filtered all images, exposure maps, and event files using `dmcopy` to only include the data covering the GC up to 1.2 times the half-light radius. The factor of 1.2 is a rather conservative upper limit to consider uncertainties in measurements of half-light radii and GC center coordinates. We used GC center coordinates and half-light radii from the Harris catalog (2010 edition, Harris 1996) to apply this cut. We note that the Harris catalog coordinates for Terzan 1 appear to have a $\sim 44''$ offset from the values reported by Picard & Johnston (1995). When compared to images of the cluster, the values from Picard & Johnston (1995) appear to be more accurate (Figure 1). Thus, for this specific cluster, we used the cluster coordinates from Picard & Johnston (1995).

After restricting the observation and analysis to the region of interest, we ran `wavdetect` on each observation to produce observation-specific source catalogs (source detection is discussed in detail in Section 3.1). If there was more than one observation covering a GC, we used `merge_obs` to reproject and merge all available data on the GC. For most GCs, comparing observation-specific source catalogs indicated that the relative astrometric shifts between observations of a GC are negligible. However, this was not the case for Terzan 5 and M30. For these clusters, we used `wcs_match` and `wcs_update` to correct the relative astrometry in the event files and aspect solutions, prior to producing images and merging observations.

3. Analysis Methods

After reprocessing and preparing the Chandra/ACIS data on each cluster, we proceeded to perform source detection, followed by photometry and source evaluation in AE and spectral analysis in BXA.

3.1. Source Detection

We performed source detection on all observations/GCs by running `wavdetect` on the underbinned stacked images (binned by a factor of 0.5) of each cluster. Source detection was carried out with a broad range of scales (1, 2, 4, 8, 16) and generally liberal detection thresholds (`wavdetect`'s threshold for identifying a pixel as belonging to a source, $10^{-4} - 10^{-5}$, depending on the depth and noise level in the observations). Choosing a liberal detection threshold generally increases the number of possible false detections, while it allows sensitivity to marginal detections. We chose such a threshold in order to leave assessment of whether a source is real to a later stage in

¹¹ We note that there have been no software or calibration updates that would impact the analysis in this work significantly.

¹² <https://cxc.cfa.harvard.edu/ciao/threads/flare/index.html>

Table 1
List of All GCs and Their Chandra/ACIS Observations Reduced and Analyzed in This Work

GC	Obs.ID	Date	Exp (ks)	GC	Obs.ID	Date	Exp (ks)
Djorg 2	17844	2017 May 13	22.7	NGC 5927	08953	2008 Apr 30	7.8
M2	08960	2008 Apr 9	11.5		13673	2012 Jan 3	47.4
M4	00946	2000 Jun 30	25.8	NGC 6139	08965	2008 May 26	17.7
	07446	2007 Sep 18	47.9	NGC 6304	08952	2008 Jan 28	5.3
	07447	2007 Jul 6	45.5		11073 ^a	2010 Jul 6	97.5
M5	02676	2002 Sep 24	44.7	NGC 6325	08959	2009 Jan 29	16.7
M9	08954	2009 Jan 29	8.4	NGC 6352	13674	2012 Jun 20	19.8
M10	16714	2015 May 8	32.6	NGC 6362	11024	2009 Nov 21	30.8
M12	04530	2004 Jul 17	26.6		12038	2009 Nov 29	9.0
M13	05436	2006 Mar 11	26.8	NGC 6388	05505	2005 Apr 21	44.6
	07290	2006 Mar 9	27.9		12453 ^b	2011 Aug 29	2.5
M14	08947	2008 May 24	12.1	NGC 6397	00079 ^a	2000 Jul 31	48.3
M19	17848	2016 Jul 2	22.7		02668	2002 May 13	28.1
M22	05437	2005 May 24	15.8		02669	2002 May 15	26.7
	14609	2014 May 22	84.9		07460	2007 Jul 16	147.7
M28	02683	2002 Sep 9	14.1		07461	2007 Jun 22	88.9
	02684	2002 Jul 4	12.8	NGC 6522	03780 ^a	2003 Jul 9	96.5
	02685	2002 Aug 4	13.5		08963	2008 Oct 27	8.3
	09132	2008 Aug 7	142.3	NGC 6539	08949	2008 Oct 31	15.0
	09133	2008 Aug 10	54.5	NGC 6541	03779	2003 Jul 12	44.8
	16748	2015 May 30	29.7	NGC 6544	05435	2005 Jul 20	16.3
	16749	2015 Aug 7	29.6	NGC 6553	08957	2008 Oct 30	5.2
	16750	2015 Nov 7	29.6		13671	2013 Mar 15	31.5
M30	02679	2001 Nov 19	49.4	NGC 6760	13672	2012 Jun 27	51.4
	18997 ^b	2017 Sep 6	90.2	Terzan 1	05464	2005 May 10	18.9
	20725 ^b	2017 Sep 4	17.5		17847	2017 May 11	14.9
	20726 ^b	2017 Sep 10	19.2		20075	2017 May 10	13.8
	20731 ^b	2017 Sep 16	24.0	Terzan 5	03798	2003 Jul 13	39.3
	20732 ^b	2017 Sep 14	47.9		10059 ^b	2009 Jul 15	36.3
	20792 ^b	2017 Sep 18	36.9		13225	2011 Feb 17	29.7
	20795 ^b	2017 Sep 22	14.3		13252	2011 Apr 29	39.5
	20796 ^b	2017 Sep 23	30.7		13705	2011 Sep 5	13.9
M54	04448 ^a	2003 Sep 1	29.8		13706	2012 May 13	46.5
M55	04531	2004 May 11	33.7		14339	2011 Sep 8	34.1
M62	02677	2002 May 12	62.3		14475 ^b	2012 Sep 17	30.5
	15761 ^b	2014 May 5	82.1		14476 ^b	2012 Oct 28	28.6
M92	03778	2003 Oct 5	29.7		14477 ^b	2013 Feb 5	28.6
	05241	2003 Oct 19	22.9		14478 ^b	2013 Jul 16	28.6
M107	17845	2016 Jun 28	11.8		14479 ^b	2014 Jul 15	28.6
NGC 2808	07453 ^a	2007 Jun 19	45.4		14625	2013 Feb 22	49.2
	08560 ^a	2007 Jun 21	10.8		15615	2013 Feb 23	84.2
NGC 3201	11031	2010 Sep 22	83.5		15750	2014 Jul 20	23.0
NGC 4372	17843	2016 Jun 25	10.3		16638	2014 Jul 17	71.6
NGC 4833	17846	2017 Jan 3	11.8		17779	2016 Jul 13	68.8
					18881	2016 Jul 15	64.7

Notes.

^a Indicates that the observation was taken with the target on ACIS-I (as opposed to ACIS-S).

^b Indicates the observation was taken in subarray mode.

AE, which allows a more rigorous verification in the photon-starved regime.

Merging multiple data sets generally produces deeper data; however, in some cases it produced suboptimal results. For example, in one of the two Chandra/ACIS observations of M62 (Obs. ID 02677), the cluster core is $\sim 2.4'$ off-axis, while it is on-axis in the other observation (Obs. ID 15761). Thus, merging these two observations produced artifacts caused by the different PSFs. This is a particularly important issue for M62, as the cluster contains numerous X-ray sources in its core. This issue is also present in observations covering NGC 6522, where the first observation (Obs. ID 03780) targets

Baade's window, but also covers this cluster at a highly off-axis angle. In these cases, instead of producing a source catalog based on the merged image, we cross-matched source catalogs from the two observations to produce a complete source catalog.

Another issue affecting some GCs was the presence of faint outbursts. While we excluded observations in which a bright outburst (or persistent emission) from an XRB prevented effective inspection of faint sources in the cluster, we did include observations where outbursts were sufficiently faint to allow detection of faint sources in the GC to some level. Only two observations were affected by this issue (one for Terzan 5

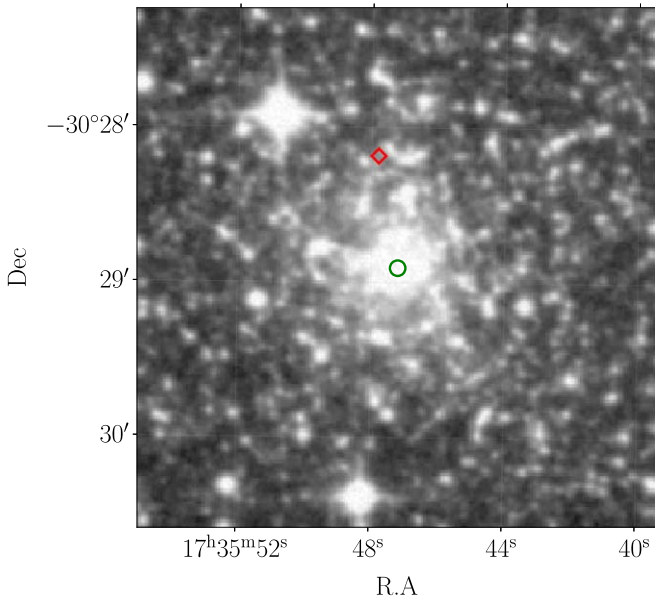


Figure 1. Digitized Sky Survey (DSS) image of Terzan 1 and comparison of GC coordinates from the Harris catalog (red diamond) to the values from Picard & Johnston (1995, green circle).

and one for NGC 6388). In both cases, the effect of the contaminated observations was small, particularly as the rest of the data covering these clusters were relatively deeper.

After producing observation-specific and merged source catalogs for each GC, we visually inspected the images and detected sources to evaluate the quality of the stacked images and search for clear sources that were missed by the algorithm, especially in crowded regions (where `wavdetect` has difficulty picking apart two sources close together). If there were obvious sources that were missed after fine-tuning the source detection parameters (e.g., detection threshold in `wavdetect`), we made a catalog of these sources manually for each cluster, with coordinates estimated based on rough centroid coordinates. These manually added input catalogs were only produced for six GCs and contain a total of 31 sources together. These consist of 10 possible sources in Terzan 5, 10 in M62, eight in M28, and one in each of M30, M92, and NGC 6397. These catalogs provide an additional list of sources for verification and analysis in AE.

After producing filtered event files, aspect solutions, exposure maps through CIAO, and source catalogs as described above, we passed these as input to AE to evaluate source properties, extract light curves and spectra, and perform spectral analysis (with BXA).

3.2. Source Evaluation and Photometry

We used AE (version 2018feb6) to assess source significance, enhance source localization, extract source-specific products (e.g., event lists, light curves, spectra and associated files), and perform photometry. We followed the general recipe provided in the AE manual¹³ for point sources, with some modifications, as detailed below.

Background extraction is a crucial component for most parts of our analysis (source validation, photometry, and spectral analysis) and it requires additional care. AE provides multiple

methods for selection of a background region based on the complexity of the emission and sources in the field. In most cases, we used circular regions with model-based masking produced via `ae_better_masking` (selecting larger masks for brighter sources and smaller masks for faint sources). However, in cases of crowded fields, this method can produce unusually large background regions with almost all local background ignored under masks. Thus for GCs where crowding is a possible issue (M28, M30, M62, M92, NGC 6388, NGC 6397, NGC 6541, and Terzan 5), we used model-based background regions produced with `ae_better_backgrounds`. This iterative (and rather computationally expensive) method attempts to achieve a balance between sufficient background counts and the “compactness” of the region. Additionally, it considers the effect of the PSFs of nearby sources on a background region through modeling of the PSF. We also made sure that the backgrounds are always extracted from the same chip as the source.

We merged observations, extracted source products, and performed photometry in five different bands (0.5–8, 0.5–2, 2–8, 0.5–10, 1–10 keV) using `MERGE_OBSERVATIONS` in AE, while choosing the flag `MERGE_FOR_PB`, which optimizes the merge for source validity. This option increases sensitivity to faint variable sources, at the cost of an increased detection significance for possibly false sources (Broos et al. 2010).

Lastly, we used `FIT_SPECTRA` to fit the spectra with an absorbed power law. This fit was done as a quick benchmark and to obtain rough estimates on the absorbed flux in different bands. As described in Section 3.3, we perform a robust spectral analysis through BXA.

3.2.1. The Special Case of Terzan 5

Terzan 5 stands out as a unique cluster in the X-rays. With the highest number of X-ray sources detected in any GC (e.g., Heinke et al. 2006b), crowding poses a serious issue in the core of this cluster. Additionally, Terzan 5 contains the highest number of pulsars detected in any GC (38 discovered so far; e.g., Lyne et al. 2000; Ransom et al. 2005; Cadelano et al. 2018). Several of these pulsars do have X-ray counterparts. Thus, careful disentangling, detection, and localization of sources in this cluster are crucial. We note that Cheng et al. (2019a) recently produced a careful study of the population and distribution of X-ray sources in Terzan 5 as this work was in the late stages of preparation. Given their focus on the radial distribution of sources and our interest in careful consideration of MSP X-ray counterparts, we retain this cluster in our analysis.

For Terzan 5, we first corrected the absolute astrometry using the source catalog from Heinke et al. (2006b). For input source catalogs, we made four nonoverlapping source catalogs. In addition to `wavdetect`, we also performed source detection using `PWDETECT`¹⁴ (Damiani et al. 1997), as it is particularly powerful in the detection of faint sources in crowded regions. We then removed overlapping sources from `PWDETECT` that had already been detected by `wavdetect`. We proceeded to compare this source catalog against the catalog of pulsars in Terzan 5 (Ransom et al. 2005), and if a pulsar was not detected by `Wavdetect` or `PWDETECT`, we added it to the input catalog for AE (a complete study of MSPs in Terzan 5 will be reported in S. Bogdanov et al. 2020, in

¹³ http://personal.psu.edu/psb6/TARA/ae_users_guide.html

¹⁴ http://cerere.astropa.unipa.it/progetti_ricerca/PWDETECT/

preparation). Lastly, we visually inspected the core of the cluster and added a total of 10 marginal sources, which were not picked up by the detection algorithms.

3.3. Spectral Analysis

After extracting and producing source and background spectra and associated files via AE, we performed a thorough and automated spectral analysis of all sources. First, we performed basic spectral fitting for all detected sources with an absorbed power law using AE and Xspec (Arnaud 1996) to naively estimate absorbed and unabsorbed flux for every source in multiple bands. However, for robust modeling, with careful consideration of uncertainties and the possibility of careful model comparison, we implemented the Bayesian framework provided by BXA¹⁵ (Buchner et al. 2014), which connects the nested sampling algorithm MULTINEST (Feroz et al. 2019) with the fitting environment PyXspec¹⁶ (Arnaud 1996) for spectral analysis. MultiNest allows efficient exploration of the parameter space in high dimensions, which may contain multiple modes through uncorrelated samples.

We fit the stacked 0.3–10 keV X-ray spectrum of each source with W-stats statistics (Cash 1979). We binned each stacked spectrum to contain at least one background count per spectral bin using the task `ftgrouppha` in HEASOFT. This is to address a possible bias in some applications of W-stats¹⁷. We fit the spectra with three different models: absorbed power law (TBABS \times PEGPWRLW), absorbed blackbody (TBABS \times CFLUX \times BBODYRA.D), and absorbed diffuse gas emission (TBABS \times CFLUX \times APEC). Xspec’s multiplicative component CFLUX was added for a robust constraint on unabsorbed flux (PEGPWRLW’s normalization is already calibrated to yield model flux, so CFLUX was not needed in that case). In all spectral analyses, we assumed Wilms et al. (2000) abundances of elements and Verner et al. (1996) photoelectric cross sections. We assumed uniform priors on the power-law photon index (between -1 and 4) and the $\log_{10}\text{Flux}$ parameter in CFLUX (between -17 and -8). We assumed log-uniform priors for all other parameters to allow scale invariance over multiple orders of magnitude: N_{H} between 10^{19} and 10^{24} cm^{-2} , kT_{APEC} between 0.008 and 30 keV, and kT_{BB} between 0.001 and 10 keV. Finally, we used model evidence ($\log_{10}Z$ as implemented in BXA) to compare the three different models for each source.

4. Catalog of X-Ray Sources in Galactic Globular Clusters

We produced a catalog of X-ray sources in 38 GCs through the steps explained in Sections 2 and 3, with measurements of numerous observational properties of these sources. The complete catalog is available in the electronic version of this article in the Appendix. In the Appendix, we also provide a complete overview of catalog entries/column available for each source. In this section, we describe in detail how the catalog was developed and vetted and provide an overview of various observed properties for cluster sources.

¹⁵ <https://johannesbuchner.github.io/BXA/>

¹⁶ <https://heasarc.gsfc.nasa.gov/docs/xanadu/xspec/python/html/index.html>

¹⁷ See Appendix B in the XSPEC manual: <https://heasarc.gsfc.nasa.gov/xanadu/xspec/manual/XSAppendixStatistics.html>.

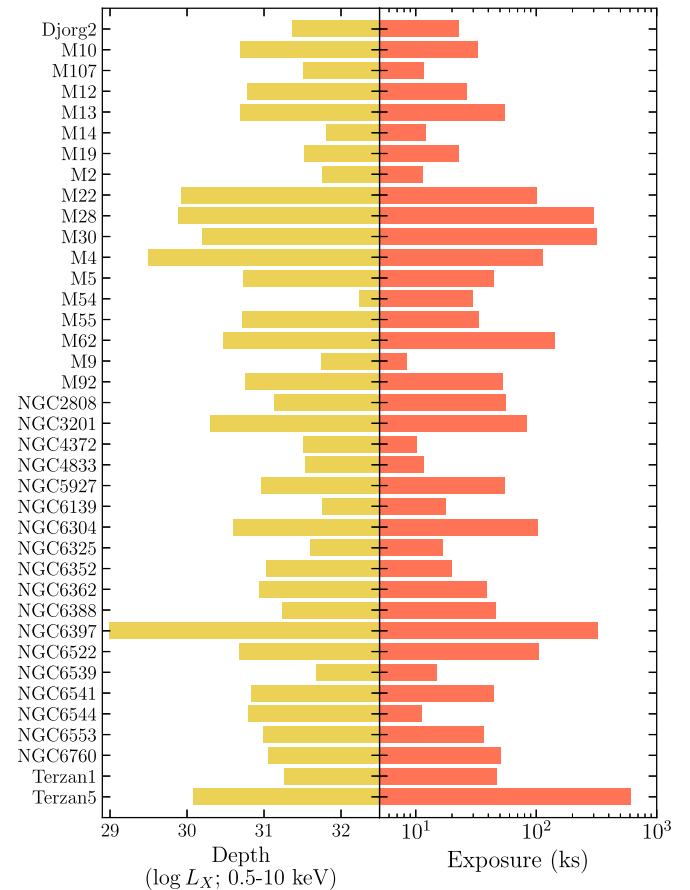


Figure 2. Coverage and “depth” of Chandra/ACIS observations for the clusters in our sample. Depth is calculated based on X-ray luminosity (in erg s^{-1}) of a hypothetical source with five net counts, with an absorbed power-law spectrum (with the GC’s N_{H} and a photon index of 1.7) over the total GC exposure time.

4.1. Catalog Depth and Sensitivity

GCs in our sample are not observed uniformly in the X-rays. Some of these clusters have been observed for hundreds of kiloseconds, while some have only been observed for far shorter exposure times (Figure 2). This dispersion in depth only gets stronger when the effects of variable interstellar absorption and distance are considered. Thus, it is important to estimate a sensitivity limit for each cluster by taking the above factors into account.

We estimate a measure of X-ray flux sensitivity for each GC, assuming we can confidently detect an X-ray source with five net counts (in the 0.5–10 keV band) over the total exposure time for the GC with the primary CCD (Chandra/ACIS-S or Chandra/ACIS-I) in the primary Chandra cycle. We define the primary CCD and cycle as the ones used in the majority of the observations. We need to consider the CCD and observing cycle that most of the GC observations were taken in because of sensitivity differences between Chandra/ACIS-S or Chandra/ACIS-I and impacts of contamination on Chandra/ACIS detectors over time.¹⁸ Thus, we use PIMMS¹⁹ to estimate the unabsorbed flux corresponding to a net count of five for each GC. We assume a typical power-law spectrum with a photon index of 1.7, and each cluster’s expected hydrogen column

¹⁸ <https://cxc.harvard.edu/ciao/why/acidsecontamN0010.html>

¹⁹ <https://asc.harvard.edu/toolkit/pimms.jsp>

Table 2
Estimation of Depth and Sensitivity for the GCs in Our Sample

GC	Exposure (ks)	Prim. CCD	Prim. Cycle	GC N_{H} (cm^{-2})	GC Distance (kpc)	Lim. Unabs. Flux ($\text{erg s}^{-1} \text{cm}^{-2}$)	Lim. L_{x} (erg s^{-1})	No. Sources
Djorg 2	22.7	7	17	8.19×10^{21}	6.3	4.91×10^{-15}	2.32×10^{31}	2
M2	11.5	7	09	5.23×10^{20}	11.5	3.64×10^{-15}	5.75×10^{31}	5
M4	113.9	6,7	08	3.05×10^{21}	2.2	5.37×10^{-16}	3.10×10^{29}	100
M5	44.7	7	03	2.61×10^{20}	7.5	7.84×10^{-16}	5.26×10^{30}	13
M9	8.4	7	09	3.31×10^{21}	7.9	7.48×10^{-15}	5.56×10^{31}	1
M10	32.6	7	16	2.44×10^{21}	4.4	2.13×10^{-15}	4.91×10^{30}	13
M12	26.6	7	05	1.66×10^{21}	4.8	2.19×10^{-15}	6.02×10^{30}	6
M13	54.7	7	06	1.74×10^{20}	7.1	8.02×10^{-16}	4.82×10^{30}	18
M14	12.1	7	09	5.23×10^{21}	9.3	6.26×10^{-15}	6.45×10^{31}	5
M19	22.7	7	17	3.31×10^{21}	8.8	3.56×10^{-15}	3.29×10^{31}	4
M22	100.7	6,7	15	2.96×10^{21}	3.2	6.77×10^{-16}	8.26×10^{29}	80
M28	300.5	7	09	3.48×10^{21}	5.5	2.13×10^{-16}	7.66×10^{29}	136
M30	307.5	7	18	2.61×10^{20}	8.1	2.00×10^{-16}	1.57×10^{30}	20
M54	29.8	3	04	1.31×10^{21}	26.5	2.04×10^{-15}	1.70×10^{32}	7
M55	33.7	6,7	05	6.97×10^{20}	5.4	1.48×10^{-15}	5.15×10^{30}	17
M62	142.4	7	15	4.09×10^{21}	6.8	5.33×10^{-16}	2.94×10^{30}	74
M92	52.6	7	04	1.74×10^{20}	8.3	6.88×10^{-16}	5.65×10^{30}	12
M107	11.8	6,7	17	2.87×10^{21}	6.4	6.58×10^{-15}	3.21×10^{31}	4
NGC 2808	56.2	1,3	08	1.92×10^{21}	9.6	1.23×10^{-15}	1.36×10^{31}	13
NGC 3201	83.5	7	11	2.09×10^{21}	4.9	7.01×10^{-16}	2.00×10^{30}	32
NGC 4372	10.3	6,7	17	3.40×10^{21}	5.8	7.91×10^{-15}	3.17×10^{31}	7
NGC 4833	11.8	7	17	2.79×10^{21}	6.6	6.53×10^{-15}	3.39×10^{31}	2
NGC 5927	54.5	7	13	3.92×10^{21}	7.7	1.31×10^{-15}	9.26×10^{30}	11
NGC 6139	17.7	7	09	6.53×10^{21}	10.1	4.72×10^{-15}	5.74×10^{31}	7
NGC 6304	102.5	1,2,3	11	4.70×10^{21}	5.9	9.65×10^{-16}	4.00×10^{30}	23
NGC 6325	16.7	7	09	7.93×10^{21}	7.8	5.50×10^{-15}	3.99×10^{31}	5
NGC 6352	19.8	7	13	1.92×10^{21}	5.6	2.86×10^{-15}	1.07×10^{31}	10
NGC 6362	38.7	7	11	7.84×10^{20}	7.6	1.23×10^{-15}	8.49×10^{30}	17
NGC 6388	46.7	7	06	3.22×10^{21}	9.9	1.49×10^{-15}	1.74×10^{31}	36
NGC 6397	325.1	0,6,7	08	1.57×10^{21}	2.3	1.55×10^{-16}	9.76×10^{28}	124
NGC 6522	104.0	2,7	04	4.18×10^{21}	7.7	6.74×10^{-16}	4.76×10^{30}	10
NGC 6539	15.0	7	09	8.89×10^{21}	7.8	6.48×10^{-15}	4.70×10^{31}	7
NGC 6541	44.8	7	04	1.22×10^{21}	7.5	1.02×10^{-15}	6.83×10^{30}	27
NGC 6544	16.3	7	06	6.62×10^{21}	3.0	5.78×10^{-15}	6.20×10^{30}	6
NGC 6553	36.7	7	13	5.49×10^{21}	6.0	2.23×10^{-15}	9.57×10^{30}	18
NGC 6760	51.4	7	13	6.71×10^{21}	7.4	1.75×10^{-15}	1.14×10^{31}	12
Terzan 1	47.3	6,7	17	1.73×10^{22}	6.7	3.41×10^{-15}	1.82×10^{31}	67
Terzan 5	597.0	7	15	2.07×10^{22}	5.9	2.85×10^{-16}	1.18×10^{30}	188

Note. Primary CCD and primary cycle refer to the Chandra/ACIS CCD (ACIS-I or ACIS-S) and Chandra observation cycle that most or all of a GC’s observations were taken in. Cluster N_{H} and distance values are based on the Harris catalog. The limits on unabsorbed flux and X-ray luminosity are estimated in the 0.5–10 keV band for a source with five net counts over the GC total exposure, assuming a power-law spectrum with a photon index of 1.7 (see text). No. Sources represents the number of confident sources identified in each cluster (above the estimated threshold within the extraction region for each cluster, $\sim 1.2 \times R_{\text{hl}}$).

density (based on optical reddening values reported in the Harris catalog and following the correlation reported by Bahramian et al. 2015; Foight et al. 2016). Finally, we use the GC distance to estimate the corresponding X-ray luminosity. These depth estimations are tabulated in Table 2 and are demonstrated in Figure 2. The median depth is $L_{\text{x}} \sim 9 \times 10^{30} \text{ erg s}^{-1}$.

It is worth noting that these estimates are just first-order approximations and are not hard cutoff thresholds. Variable backgrounds, off-axis angles, and spectral shapes are issues that this estimation does not address. However, these issues are unlikely to have large impacts in most cases. The GC most vulnerable to these issues is Terzan 5, where the high absorption severely extinguishes the sources at $L_{\text{x}} < 10^{31} \text{ erg s}^{-1}$ (and reduces the count rate for fainter sources more than for brighter sources on average, since fainter sources tend to be softer; e.g., Heinke et al. 2006b), and the crowding in the core increases the

probability of missing sources in the high local background caused by the PSF wings of nearby sources.

4.2. Source Validity

As mentioned in Section 3.1, we chose moderately liberal detection thresholds in our initial source detection with `wavdetect` (with `sigthresh` typically set to 10^{-4} or 10^{-5}), with a plan to better estimate our confidence of source detection with AE and carefully consider the PSF and local background in this second round. AE estimates source “significance” and a measure of false detection probability (“`prob_no_source`”) based on total source counts and background counts in the Poisson regime, following the method by Weisskopf et al. (2007). We estimated this probability in five different bands (0.5–8, 0.5–2, 2–8, 0.5–10, and 1–10 keV) for each source to increase sensitivity to faint sources that are

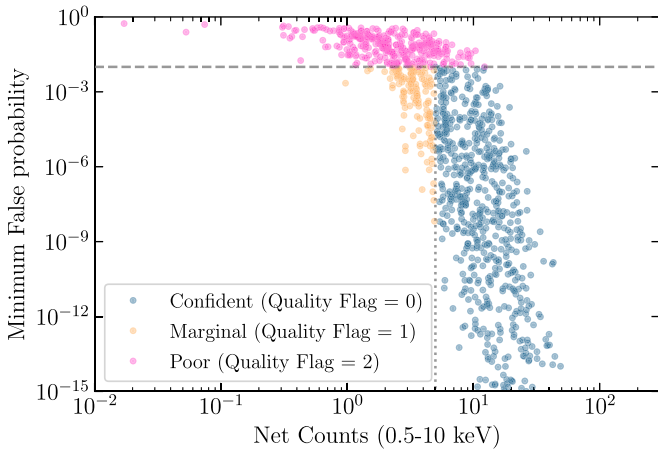


Figure 3. Detection quality thresholds in the catalog. With these thresholds, our catalog contains 1139 confident, 134 marginal, and 394 poor detections. Note that there are numerous sources outside the plotted range with smaller (≈ 0) false probabilities.

extremely soft or hard. It is important to note that there are no simple “number of independent trials” that can be associated with the significance and probability measured this way by AE.²⁰

We do not remove any of the originally detected sources from our catalog. However, based on source net counts (in the 0.5–10 keV band) and the minimum false probability (minimum probability across the different bands), we assign a detection quality flag to each source. If a source has a minimum false probability value of $\geq 1\%$, we classify it as a poor detection (with a detection quality flag value of 2). If a source has a minimum false probability value of $< 1\%$ and a net source count < 5 (in the 0.5–10 keV band), we classify it as a marginal detection (detection quality flag value = 1). Finally, if a source has a minimum false probability value of $< 1\%$ and a net source count ≥ 5 , we classify it as a confident detection (detection quality flag value = 0; Figure 3). The choice for a hard threshold of 5 on the net counts is partially arbitrary. However, it is somewhat informed by the fact that it is uncommon for a Chandra detection with < 5 net counts to be robust without any other prior evidence (especially in the presence of a strong background). Additionally, this choice allows estimates of reasonable flux sensitivity floors for each GC, assuming a minimum number of counts and given the accumulated Chandra exposure of the cluster (as detailed in Section 4.1).

Marginal and poor detections provide useful information about the sensitivity and robustness of our catalog. Furthermore, the false probabilities of these sources may be reevaluated in the presence of external evidence (e.g., evidence of an interesting source at a given position in multiwavelength observations).

With these classifications, this catalog contains 1139 confident, 134 marginal, and 394 poor detections. These classifications are reflected in the catalog under the column “detection_quality_flag,” and source significance and false probabilities in all five bands are reported under columns “significance” and “prob_no_source,” respectively.

²⁰ AE manual, Section 5.10.3: http://personal.psu.edu/psb6/TARA/ae_users_guide.html.

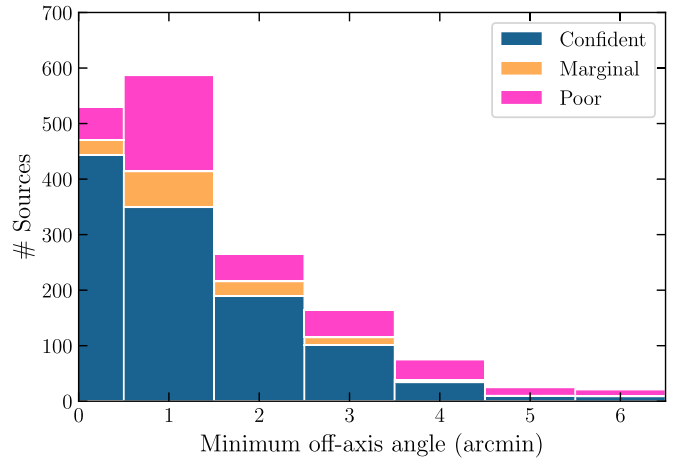


Figure 4. Distribution of minimum off-axis angles in our catalog. Note that 17% of all sources in the catalog are observed only at off-axis angles larger than $2\prime.5$.

4.3. Source Coverage and Extraction

For most of the sources in the catalog, all observations of their host GC cover these sources in a uniform fashion. However, some sources reside on the outskirts of large GCs, can fall on the chip gap (or fall off subarrays) in one or more observations, or can be impacted by large off-axis angles. Thus it is important to carefully consider which observations to merge to obtain optimized products. AE allows a systematic source-by-source merge of overlapping observations to allow optimization for a specific goal (e.g., maximizing source validity, enhancing source position precision, or enhancing the signal-to-noise ratio (S/N) for photometry and spectroscopy) in the MERGE stage. We chose to merge, aiming to maximize source validity. For most of the sources in the catalog (1429 out of 1667), this choice yields a stack of all observations covering an individual source. The total number of observations used to produce merged products for each source are reported under columns “num_obs_total” and “num_obs_merged.”

We also include the range of off-axis angles at which each source has been observed (under columns “theta_low,” “theta_avg,” and “theta_high”), total on-source exposure time, and the primary Chandra/ACIS CCD covering each source (which is ACIS-S3 for all but 156 sources). Most of the sources in our catalog are observed at low off-axis angles at least once, but $\sim 17\%$ of the sources have been observed only at off-axis angles larger than $2\prime.5$ ²¹ (Figure 4).

Off-axis angle and primary CCD are important attributes to consider when investigating individual sources. As we discuss in the next section, large off-axis angles can produce additional uncertainty in localization.

4.4. Source Localization and Astrometry

AE provides three methods to estimate source localization. The most basic method is via the mean position of events in a specified band, with uncertainties estimated as the standard error of the mean. AE developers note that the mean position

²¹ An off-axis angle of $2\prime.5$ is roughly where distortion of the Chandra/ACIS PSF becomes significant (e.g., see https://cxc.harvard.edu/ciao/PSFs/psf_central.html).

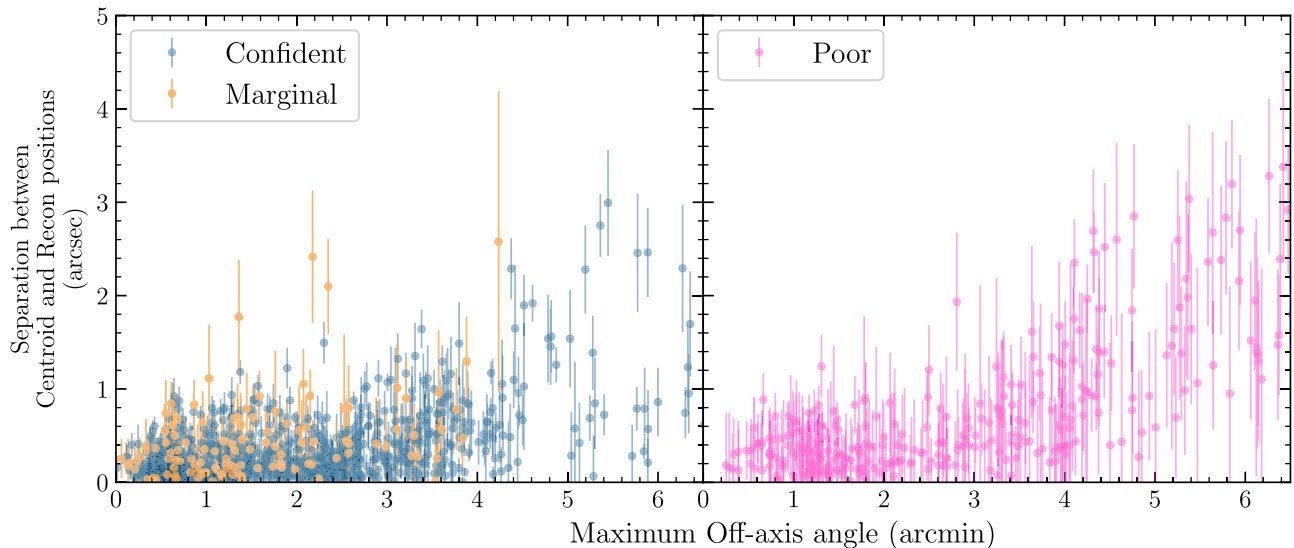


Figure 5. Discrepancy between localizations based on centroiding and reconstruction vs. off-axis angles. The discrepancy is negligible at low off-axis angles, but becomes important at large off-axis angles. The error bars plotted on the y-axis are the uncertainties on centroid localization.

calculated this way²² may be biased when the PSF is asymmetric (e.g., at high off-axis angles) or when the background is nonuniform and “sloped” (e.g., when near a bright source). AE provides two other methods of estimating the source position. One of these methods estimates the position by correlating the neighborhood around the source with the source’s PSF. This method may also be biased in the presence of a nonuniform local background. Thus, AE provides a third method for estimating position based on image reconstruction and peaks. Unfortunately, currently there are no estimations of uncertainties available for correlation- and reconstruction-based localization methods.

Given the large number of sources in the catalog and the spread in data quality, background, crowding, and off-axis angles, it is difficult to systematically choose a best localization method for each source. Thus we provide localization for each source via all three methods in the catalog. It is worth noting that while correlation- and reconstruction-based localizations are expected to provide more accurate estimates, especially at high off-axis angles, we notice that this may not be the case all the time. Therefore, we chose to extract products (light curve, spectra, and so on) for all sources based on the mean positions (the first method provided by AE). In most cases, the discrepancy between different localization methods has a negligible impact on these products (especially for confident detections), but not always. As demonstrated in Figure 5, discrepancies between different localization methods are negligible at low off-axis angles for sources with sufficient counts. However, at large off-axis angles, this issue becomes important.

Thus, we urge the user to check localizations for their sources of interest, along with the extraction region used, the source’s off-axis angle, and crowding in the vicinity of the source. As described in Section 4.7, we provide figures and plots for each source to check these visually for each source in the catalog.

4.5. Photometry and Variability

We perform photometry (and source validation) in five bands (0.5–2, 2–8, 0.5–8, 0.5–10, 1–10 keV) for all sources using

AE. As discussed in detail in the AE documentation (Section 5.6.3), adjusting the background scaling is a crucial step in gaining photometric accuracy and more robust source validity. We follow the suggestions for this technique and readjust the background scale iteratively, and then we perform photometry and source validation. We report source counts, background counts, background scaling factor, background-subtracted “net” counts, and uncertainties on the net counts as estimated following Weisskopf et al. (2007) in all of the aforementioned bands.

AE also provides Kolmogorov–Smirnov (K-S; Kolmogorov 1933; Smirnov 1948) and χ^2 tests, and their associated p -values, for source variability within and between observations. Given that a majority of our sources are in the low-count regime (and thus do not have Gaussian uncertainties on count rates), we neglect the χ^2 test altogether and only include the K-S test p -values for variability within and between observations in the catalog. The p -values for variability within an observation are the minimum value among the observations. The p -values closer to zero indicate a higher probability of variability. It is worth noting that large p -values merely indicate inconclusive evidence on variability in the examined data. As we warn in Section 5.1, these values should be interpreted with caution.

4.6. Spectral Analysis

We provide the results of our spectral analysis (as explained in Section 3.3). These results include absorbed and unabsorbed flux values in different bands as estimated via AE (through the flux task in Xspec), assuming a simple power-law fit. We also list the median and 10% and 90% quantiles of the parameter posterior distributions resulting from fitting three separate models: an absorbed power law, absorbed blackbody, and absorbed diffuse plasma (APEC) in BXA and XSPEC. We also provide the unabsorbed X-ray flux and X-ray luminosity (assuming the source is in the GC) for each model in the 0.5–10 keV band. Finally, we give the relative model probability (with the probability for the most likely model set to 1.0) as estimated based on model evidence, and we indicate the best model based on these probabilities.

²² AE manual, Section 5.3.

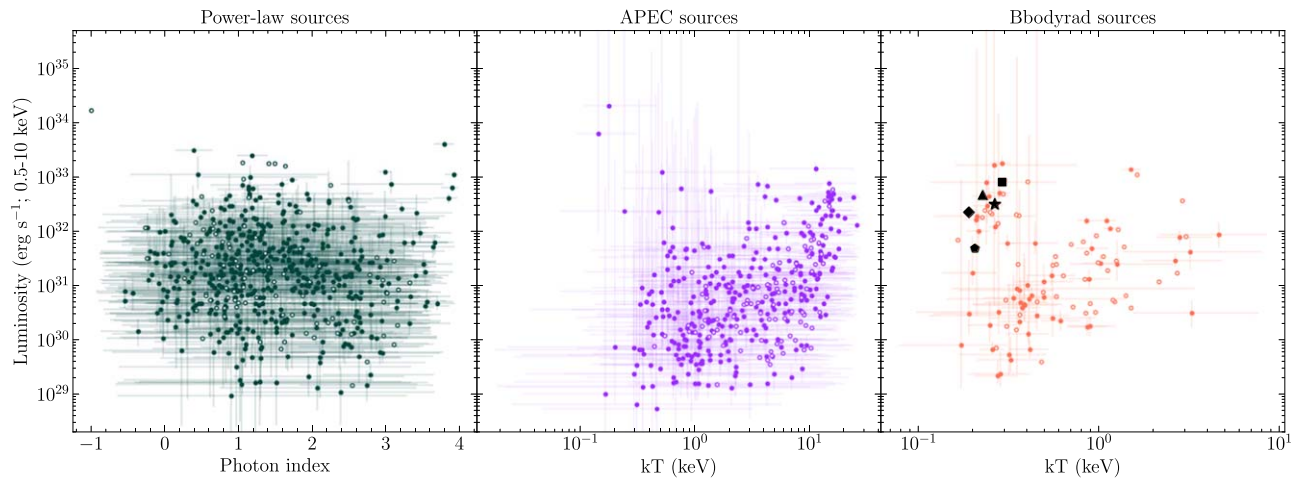


Figure 6. Overview of the spectral fitting results for the confident sources. Each source is plotted only in the panel representing the best-fit model. Luminosities are estimated assuming the source is at its host GC distance. Hollow points represent possible foreground sources, based on comparing the best-fit N_{H} for the source to the N_{H} expected for the GC (see Section 4.7). There are 620 sources best fit with a power law, 409 sources best fit by an APEC model, and 110 sources best fit by a blackbody. The black markers represent some of the known quiescent NS-LMXBs in our sample, including CXOU J214022.17–231046.2 in M30 (black triangle), CXOU J164143.76+362757.9 in M13 (black diamond), CXOU J182432.81–245208.5 in M28 (black square), CXOU J174041.48–534004.5 in NGC 6397 (black pentagon), and CXOU J171432.95–292748.1 in NGC 6304 (black star).

For completeness and comparison, we also provide the expected hydrogen column density toward the host GC, estimated based on the correlation between N_{H} and A_V (Bahramian et al. 2015; Foight et al. 2016), using the $E(B - V)$ values from the Harris catalog and assuming $R_V = 3.1$. We also estimate the uncertainties on the GC N_{H} values, considering the reported uncertainties on $E(B - V)$ in the Harris catalog, considering the reported uncertainty on the correlation slope by Bahramian et al. (2015), and assuming an uncertainty of 0.1 on R_V . We do not use these values for fitting, but as discussed in the next section, they provide a naive indicator to distinguish some foreground sources.

The results of spectral fitting for the confident detections are plotted in Figure 6. It is worth noting that the sources with a blackbody as the best-fit model include some of the well-studied known quiescent NS-LMXBs (e.g., see Guillot et al. 2013; Steiner et al. 2018) among dozens of other sources, indicating a great potential in this model selection for identification and study of new NS-LMXBs.

4.7. Flags, GC-associated Aspects, and Convenience Plots

We provide a number of columns in the final catalog to allow easy assessment of source conditions. The column “detection_quality_flag” indicates the robustness of the detection based on source net counts and validity (as explained in Section 4.2). The “spectrum quality flag” is merely based on the total number of source counts: if a source has $\gtrsim 100$ counts, it would have a relatively reliable spectral analysis (and we assign a flag value of 0). If the total number of counts is somewhere between $\lesssim 100$ and $\gtrsim 20$, the estimates are less reliable and should be taken with caution (flag value of 1). Lastly, if a source has $\lesssim 20$ counts, spectral analysis is merely suggestive, and the model comparison is not to be taken with confidence (flag value of 2).

We also provide a simple assessment of whether a source *could* be a foreground object. This assessment relies on a comparison of the 90% upper limit on a source’s N_{H} (from the best-fit model) when compared to the GC’s expected N_{H} . If a source’s N_{H} upper limit is lower than the GC N_{H} , there is a chance that it may be a possible foreground object. We emphasize that this is only a

zeroth-order suggestive indicator, and a “False” value for the “foreground_flag” does not rule out a foreground nature entirely, and a “True” value, especially for significantly bright sources, may be a result of incomplete or inaccurate spectral modeling. This flag is effective for identification of faint foreground objects in the direction of highly absorbed GCs (like Terzan 5, e.g., with ~ 50 possibly foreground sources), while it would not be a good indicator for low-absorption ones (like M30).

Precise astrometry corrections are a challenge in most X-ray observations. At this point, most of the GCs in our catalog do not have absolute astrometry corrections applied, meaning that the user should consider an additional $\sim 0''.8$ uncertainty based on the accuracy of Chandra’s absolute astrometry.²³ Currently, we have corrected absolute astrometry only for Terzan 5, following cross-matching sources to Heinke et al. (2006b). We hope to provide this correction for more clusters in future updates to the catalog. The status of the astrometry correction is indicated for each source (each GC) under “abs_astrometry_flag.”

Beside providing the host GC’s name, distance, expected N_{H} , and half-light radius (all based on the Harris catalog), we also provide each source’s angular distance from the cluster center, along with the number of background active galactic nuclei (AGNs) with higher flux than the source expected within the cluster half-light radius, using the approximation provided by Mateos et al. (2008). It is worth noting that the study of background AGNs is mostly done in low-extinction parts of the sky, while some of the GCs in our sample have very high extinction values, making it difficult or impossible to detect the “typical” contaminating AGNs in these GCs. To reduce the impact of this bias, we use unabsorbed flux values for our sources when calculating the Mateos et al. (2008) factor. The number of expected AGNs, along with GC half-light radius and source distance from GC center, provides a proxy for the likelihood that a source is a background AGN. We estimate a crude probability that each source is associated with the GC background, based on where the source is located in the GC (in the core or outside the core), the number of expected AGNs with similar or higher flux in the 2–10 keV band ($N_{\text{BKG}}(F_X > F_{X,\text{src}})$), and the number of detected

²³ <https://cxc.harvard.edu/cal/ASPECT/celmon/>

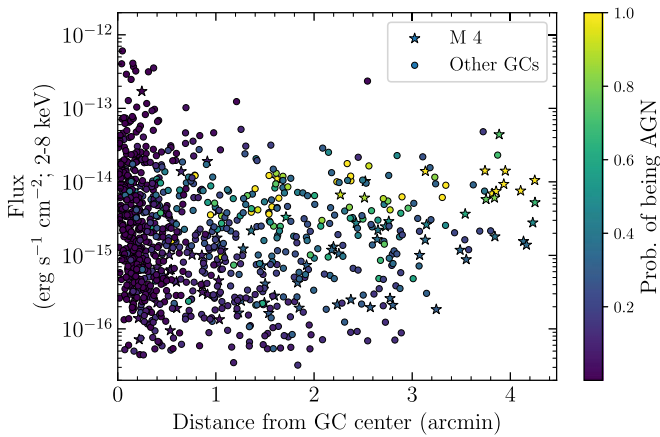


Figure 7. For all sources in our catalog, absorbed flux is plotted as a function of distance from the GC center, and points are color-coded to denote the probability of being a background AGN. Sources in M4 are highlighted because, given its nearby distance (2.2 kpc) and large half-light radius (4/3), a large number of background AGNs are expected in this cluster.

sources in that region with similar or higher flux ($N_{\text{Detect}}(F_X > F_{X,\text{src}})$). We defined the probability of being a background AGN as the ratio of $N_{\text{BKG}}(F_X > F_{X,\text{src}})/N_{\text{Detect}}(F_X > F_{X,\text{src}})$ for each source. If the source is located in the cluster core, $N_{\text{BKG}}(F_X > F_{X,\text{src}})$ and $N_{\text{Detect}}(F_X > F_{X,\text{src}})$ were estimated for the cluster core. If the source is outside the core but within the half-light radius, the estimate only includes the half-light region (excluding the core). This diagnostic affects clusters with various apparent sizes differently. For example, the number of background AGNs detected in M4, a nearby GC with a half-light radius of 4/3, which has been observed for more than 100 ks with Chandra/ACIS, would be significantly higher than in most other GCs (Figure 7). It is also worth noting that for some clusters closest to the Galactic Plane, foreground sources may be a bigger contaminant than background sources.

As an auxiliary resource, for each source we provide a compilation of plots summarizing its position within the GC and localization and extraction regions, along with plots showing the three spectral fits and parameter posterior distributions. These plots are meant to facilitate a manual assessment of individual sources and are available as a complete figure set in the online version of this article (see Figure 8 for an example) and are also accessible at <https://bersavosh.github.io/research/goose.html>.

5. Discussion

5.1. Caveats, Warnings and Pitfalls

The catalog presented in this paper is a result of a multilevel, semiautomated analysis of a large set of heterogeneous X-ray observations. Thus, there are shortcomings and caveats in the results, which we note below.

As discussed in Section 4.3, we provide multiple localizations for each source in the catalog based on available methods. It was infeasible in this work to determine the best method for each individual source without careful consideration of numerous factors (like position on the chip, crowding around the source, background profile, source brightness, and off-axis angle). Thus, we extracted all high-level *source* products (spectra, light curves, and associated files) using the centroid position. As shown in Figure 5, the difference between localization based on centroiding and image reconstruction is generally small enough that the impact on extraction of high-level products is negligible.

However, users are cautioned to check the extraction regions (as presented in convenience plots like Figure 8), especially for sources at high off-axis angles.

The catalog contains some information regarding the variability properties of individual sources. However, it is important to note that AE does not provide background-subtracted light curves and thus does not distinguish between source and background events. This issue strongly impacts the light curves (and subsequently the results of any variability tests) of sources with low numbers of counts, especially in crowded regions (e.g., the core of Terzan 5). Furthermore, while the K-S test is a strong distribution-free and easy-to-compute test, it has well-documented shortcomings (e.g., poor sensitivity in the tails of distributions; Babu & Rao 2004; Babu & Feigelson 2006; Feigelson & Babu 2012). These issues become more significant in the photon-starved regime. Thus, we advise caution in interpreting the results of variability tests and urge users to consider source brightness and the possible impact of background or nearby sources on these results.

As discussed in Section 3.3, we used Bayesian nested sampling Monte Carlo methods for spectral fitting through the BXA package on top of PYXSPEC. Given the nature of this method, it is important to consider the prior constraints on a parameter (as detailed in Section 3.3) and the shape of the posterior distribution for interpretation (i.e., whether a parameter has hit the upper or lower limit implied by the prior). The parameter posteriors are not always unimodal or quasi-Gaussian, and some parameters in a model can be strongly correlated. The auxiliary plots (available as an electronic figure set accompanying this article and also available at <https://bersavosh.github.io/research/goose.html>) include 1D and 2D histograms of posterior distributions for each model fit, to allow inspection of these issues.

It is also important to note that while our spectral fitting method provides a rather robust evaluation of parameter space, it will not overcome the intrinsic uncertainties in the extremely low-count statistics regime. For example, in some cases, spectral fitting at low S/N indicates an excessively high N_{H} , coupled with a very high X-ray luminosity (while the absorbed flux is rather low). Thus, it is important to check the uncertainty bounds and the shape of the posterior distribution at low S/N, and we urge caution in interpretation of spectral modeling results and model comparison for sources with <20 counts.

Lastly, it is worth noting that the models used for spectral analysis here are simple single-component models, and they may not be sufficiently descriptive for some sources. This is especially the case for the brightest sources with hundreds to thousands of counts; the high-S/N spectra for such sources may demand multicomponent models. Additional components may be necessary to represent system emission processes (e.g., a blackbody or an NS atmosphere model + power law for a weakly accreting NS-LMXB; see Section 5.3). Also note that the photometric and spectral analysis presented in this catalog does not include pileup corrections. Thus, it is important to consider the potential impact of pileup when using results for bright sources. AE provides an assessment of whether a source may be piled up based on PSF simulations, and we have included a flag column (named “pileup flag”) in the catalog indicating potential pileup. If this flag is “True” for a source (this occurs for only 15 sources), the spectral analysis (and assertions or flags relying on that) presented in the catalog may be inaccurate.

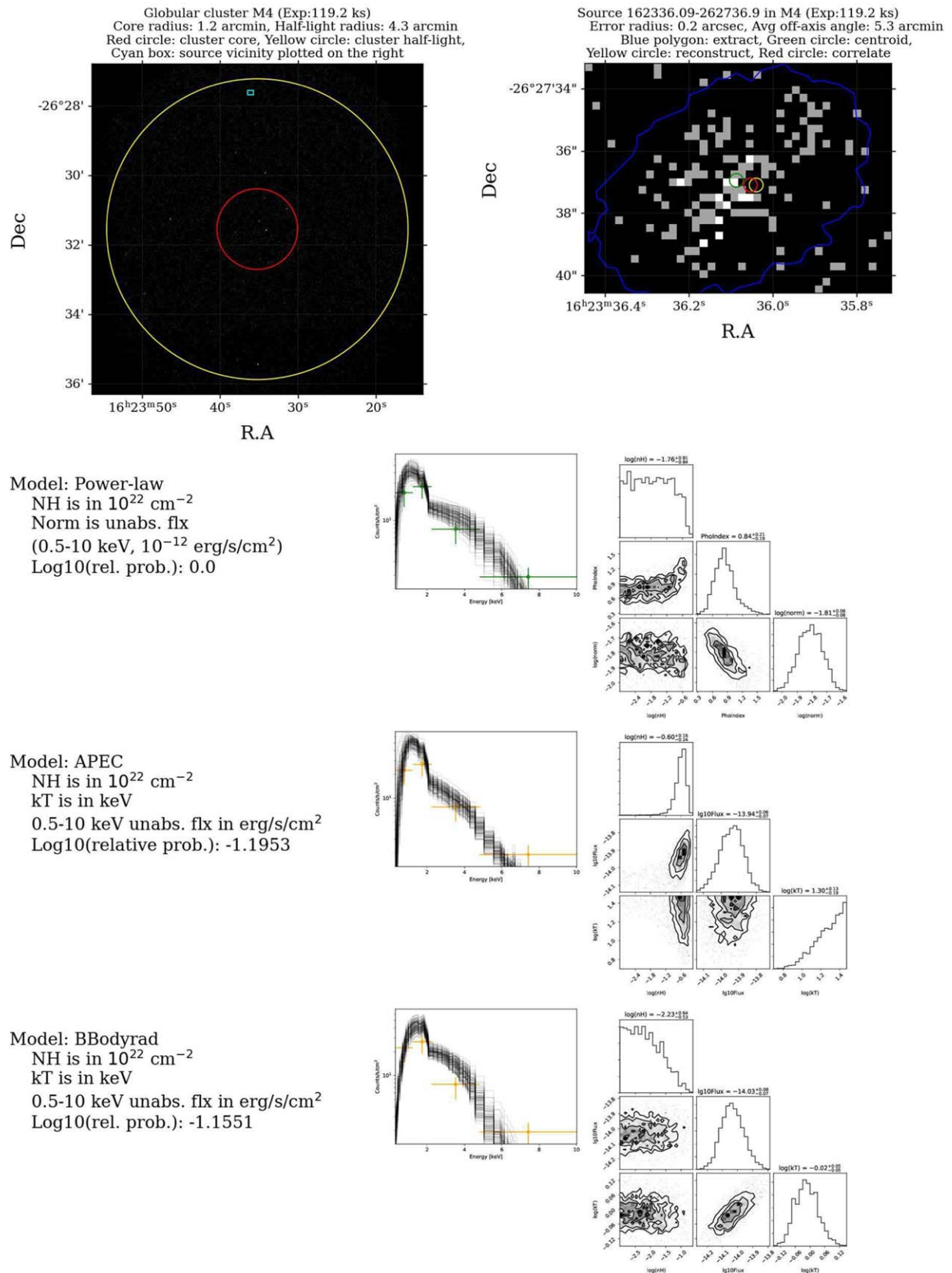


Figure 8. An example of convenience plots for a catalog source at high off-axis angle in the cluster M 4. The top left panel shows the location of the source within the cluster, to allow assessment of membership and impact of artifacts (the red circle denotes the extent of the cluster core, the yellow circle display the cluster half-light radius, and the cyan box denotes the source region. These are superimposed on the *Chandra*/ACIS image). The top right panel is a zoom-in on the source, with various localization estimates marked (as green, yellow, and red circles for the centroiding, correlation and reconstruction techniques, respectively) and the extraction region pointed out as a blue polygon. The lower panels show results of spectral fitting for each of the three models (from top to bottom: power-law, blackbody, APEC). These include a representation of the binned spectrum and the posterior sample of fits, plus a corner plot showing the posterior distribution of model parameters. A complete and high-resolution figure-set including plots for all sources in the catalog is available in the online version of this article.

(The complete figure set (1667 images) is available.)

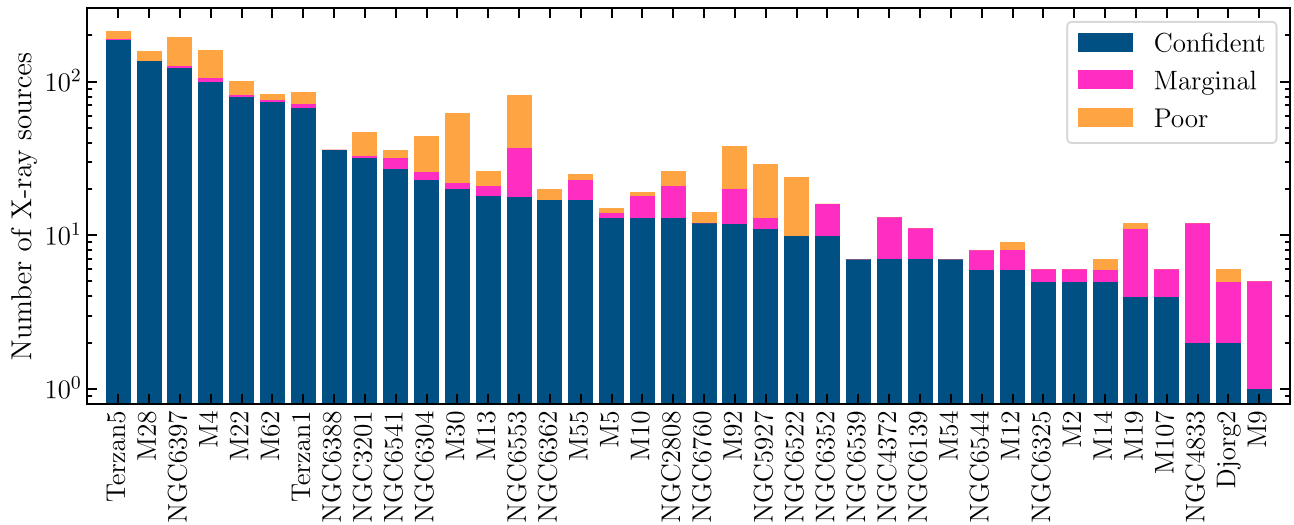


Figure 9. Number of detected X-ray sources in our catalog as a function of cluster. The numbers include sources that are likely foreground or background objects (strongly affecting GCs like M4).

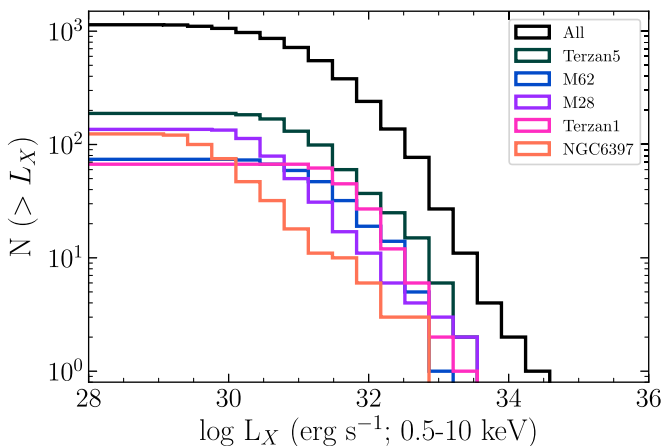


Figure 10. The cumulative X-ray luminosity distribution of X-ray sources in GCs in this study is plotted as a solid black line. Contributions of some noteworthy GCs are plotted as colored lines.

5.2. Population and X-Ray Luminosity Function of Faint X-Ray Sources in Galactic GCs

The number of observed XRBs in a GC depends on a variety of both intrinsic and observational factors, ranging from the GC’s XRB production rate to the depth of the observations and distance to the cluster. It has been established that the number of XRBs in a GC correlates strongly with the cluster encounter rate (Pooley et al. 2003; Bahramian et al. 2013).

We detect the largest number of X-ray sources toward Terzan 5, which has long been known to host a large number of XRBs and has been observed extensively. Terzan 5 is followed by M28 and NGC 6397, both of which show more than one hundred X-ray sources (Figure 9).

Using our catalog, we estimate an empirical X-ray luminosity distribution for X-ray sources with $L_X < 10^{36}$ erg s $^{-1}$ (Figure 10). For this purpose, we only consider confident detections (1139 sources). Since all GCs in our sample except for M54 are nearly complete for $L_X > 10^{32}$ erg s $^{-1}$, the luminosity distribution can be considered close to complete down to that value, with substantial incompleteness present for $L_X \lesssim 10^{31}$ erg s $^{-1}$. The caveats to the

completeness for $L_X > 10^{32}$ erg s $^{-1}$ would be any sources with heavy absorption (including partial covering) not appropriately modeled with existing data, and the possibility of a small number of sources blended in the crowded cores of M62 or Terzan 5.

However, in interpreting the luminosity distribution, it is important to consider observational biases such as the biased contribution of clusters with especially deep data. For example, sources with luminosities $< 10^{30}$ erg s $^{-1}$ are not detected in Terzan 5 due to high extinction, even though the cluster has been observed extensively. By contrast, there are numerous low-luminosity sources in the sample from nearby low- N_H GCs like NGC 6397. It is also important to note that the luminosity distribution here is heavily impacted by foreground and background sources in the direction of each GC. While the foreground flag and AGN probability provided in this catalog could in principle help with pruning out foreground and background sources, they are both very rough assessments (see Section 4.7).

5.3. Nature of the Brightest Sources in the Catalog

Typically, quiescent XRBs with main-sequence companions are observed with X-ray luminosities $\lesssim 10^{33}$ erg s $^{-1}$. However, some XRBs show brighter “quiescent” luminosities ($10^{33} \lesssim L_X \lesssim 10^{36}$ erg s $^{-1}$). Accretion at these luminosities is less well understood. Systems at these luminosities are sometimes called very faint X-ray binaries (e.g., Wijnands et al. 2006; Degenaar & Wijnands 2009). Such sources are likely to be a heterogeneous class of objects, including transitional MSPs in their subluminous disk states, symbiotic X-ray binaries (with giant companions), and other binaries with accretion at an unusually low or inefficient level for unknown reasons (e.g., Bahramian et al. 2019; Shaw et al. 2020). An advantage of the current catalog in studying these XRBs is the well-constrained distances, compared to field sources where the distance is usually unknown.

In this section, we explore the nature of sources from our catalog that have confidently measured X-ray luminosities $\geq 10^{33}$ erg s $^{-1}$ (Table 3). It is worth reiterating that the luminosities estimated in our catalog are based on the stacked spectrum for each source and thus represent average luminosities based on Chandra observations; sources that have shown a brief excursion to high luminosity in a large set of observations are unlikely to be included. First, in section Section 5.3.1 we will briefly summarize the

Table 3
Bright ($L_X > 10^{33}$ erg s $^{-1}$) XRBs in Our Catalog

CXOU J	GC	Alt. Name	PU?	D_{GC} (kpc)	L_X (10^{33} erg s $^{-1}$)	Nature	References
173617.42–444405.9	NGC 6388	IGR J17361–4441	Yes	9.9	16 ± 1	NS-LMXB?	1,2,3
173545.56–302900.0	Terzan 1	Terzan 1 CX1	No	6.7	2.5 ± 0.2	CV (IP)?	4,5
180150.32–274923.6	Djorg 2	OGLE-UCXB-01	No	6.3	2.4 ± 0.2	LMXB? IP?	6
173538.12–303032.0	Terzan 1	...	No	6.7	2.1 ± 0.3	AGN?	7
185502.95–302845.1	M54	...	No	26.5	$2.0^{+1.2}_{-0.3}$	NS-LMXB?	7
180801.98–434255.3	NGC 6541	...	Yes	7.5	$1.9^{+0.3}_{-0.2}$	NS-LMXB?	7
182432.00–245210.9	M28	PSR J1824–2452A	Yes	5.5	1.83 ± 0.04	PSR	8
174805.23–244647.3	Terzan 5	EXO 1745–248	Yes	5.9	1.79 ± 0.03	NS-LMXB	9,10,11
182432.49–245208.1	M28	IGR J18245–2452	Yes	5.5	1.70 ± 0.03	tMSP	12,13
180449.72–073526.7	NGC 6539	...	No	7.8	1.5 ± 0.2	BH-LMXB?	7
185503.47–302847.6	M54	...	No	26.5	1.4 ± 0.3	CV?LMXB?	7
174805.41–244637.6	Terzan 5	Swift J174805.3–244637	No	5.9	1.2 ± 0.1	NS-LMXB	14
162740.51–385059.1	NGC 6139	...	No	10.1	$1.1^{+0.5}_{-0.2}$	NS-LMXB?	7

Note. The “PU?” column indicates whether the Chandra data on this source may be suffering from pileup. Reported X-ray luminosities are in the 0.5–10 keV band, assuming the source is at the host GC distance. These luminosities are estimated using the best-fit models found in this work.

References. 1: Gibaud et al. (2011), 2: Pooley et al. (2011), 3: Bozzo et al. (2011), 4: Wijnands et al. (2002), 5: Cackett et al. (2006), 6: Pietrukowicz et al. (2019), 7: This work, 8: Bogdanov et al. (2010), 9: Wijnands et al. (2005) 10: Galloway et al. (2008), 11: Rivera Sandoval et al. (2018b), 12: Papitto et al. (2013), 13: Linares et al. (2014), 14: Bahramian et al. (2014).

$L_X > 10^{33}$ erg s $^{-1}$ sources in our catalog that have been previously studied in detail, and in Section 5.3.2, we will discuss sources with $L_X > 10^{33}$ erg s $^{-1}$ identified in our survey for the first time.

5.3.1. Known Systems

CXOU J173617.42–444405.9 (IGR J17361–4441) is an X-ray transient source in NGC 6388, discovered by INTEGRAL in 2011 (Gibaud et al. 2011; Wijnands et al. 2011). It had an unusually low outburst peak $L_X < 10^{36}$ erg s $^{-1}$. A comparison of Chandra observations of NGC 6388 from before the outburst to the one taken during this source’s outburst indicated a very faint quiescent level, with $L_X < 10^{31}$ erg s $^{-1}$ (Pooley et al. 2011). Based on X-ray spectroscopy and radio nondetections during the outburst, Bozzo et al. (2011) concluded that this system is likely an NS-LMXB. There have been no further outbursts detected from this cluster to date.

CXOU J173545.56–302900.0 (Terzan 1 CX1) is a bright ($L_X \sim 2 \times 10^{33}$ erg s $^{-1}$) X-ray source identified by Wijnands et al. (2002). Cackett et al. (2006) showed that the source has a very hard X-ray spectrum and may be an intermediate polar with partial covering, that is, an accreting magnetic WD with a truncated accretion disk where a subset of the X-ray emission is absorbed.

CXOU J180150.32–274923.6 (OGLE-UCXB-01) is the brightest source in Djorg 2. It has $L_X \sim 2 \times 10^{33}$ erg s $^{-1}$ and a hard X-ray spectrum. Pietrukowicz et al. (2019) identified this X-ray source as the counterpart to a variable OGLE source with a periodic modulation of 12.8 minutes. Based on the optical and X-ray properties of the system, they suggest the system might be an ultracompact XRB, harboring an NS (or a BH) accreting from a WD. However, an alternative scenario such as an intermediate polar is not ruled out.

CXOU J182432.00–245210.9 (PSR J1824–2452A) is one of seven radio MSPs in the core of M28 that show X-ray emission, and it is the X-ray brightest of these systems (Bogdanov et al. 2010). It is rather unusual for X-ray emission from radio pulsars to reach $L_X > 10^{33}$ erg s $^{-1}$: this was actually the first MSP discovered in a GC (Lyne et al. 1987) and is among the most energetic MSPs known. Bogdanov et al. (2010) argue that the

X-ray emission from this pulsar is likely due to heated magnetic polar caps.

CXOU J174805.23–244647.3 (EXO 1745–248) is a known transient X-ray burster in the core of Terzan 5, with an unusually high quiescent X-ray luminosity (Wijnands et al. 2005; Galloway et al. 2008). Study of its quiescent behavior over the last two decades with Chandra has shown extreme variability in its quiescent luminosity, ranging between 3×10^{31} and 2×10^{34} erg s $^{-1}$ (Rivera Sandoval et al. 2018b).

CXOU J182432.49–245208.1 (IGR J18245–2452; PSR J1824–2452I) in M28 is one of a handful of transitional MSP systems known (and the only one that has shown a bright X-ray outburst). The system was identified as a transitional MSP following a bright outburst in 2013, during which consistent pulsations were first detected in the X-rays and then in the radio (Papitto et al. 2013). So far, there have been three luminosity “states” observed in transitional MSPs, including a very faint ($L_X \leq 10^{32}$ erg s $^{-1}$) pulsar state, a variable subluminal ($L_X \sim 10^{33} - 10^{34}$ erg s $^{-1}$) accretion state, and a bright ($L_X > 10^{36}$ erg s $^{-1}$) outburst state (which has only been seen to date in IGR J18245–2452, Linares 2014). Chandra observations of IGR J18245–2452 (which exclude the outburst) show strong variability between 10^{32} and 10^{34} erg s $^{-1}$; most of the time, the system is in the faint accretion state with $L_X > 10^{33}$ erg s $^{-1}$ (Linares et al. 2014).

CXOU J174805.41–244637.6 is the third transient XRB discovered in the core of Terzan 5 (Bahramian et al. 2014). Detection of X-ray bursts proved the NS-LMXB nature of this system (Altamirano et al. 2012). Identification of the quiescent counterpart in Chandra observations allowed study of its long-term behavior pre- and postoutburst (Homan & Pooley 2012), indicating that the system shows a persistently high X-ray luminosity ($> 10^{33}$ erg s $^{-1}$, both before and after the outburst; Degenaar et al. 2015). This suggests that continuous low-level accretion is present in the system.

5.3.2. New Systems

A handful of bright systems in Table 3 have not been previously studied in detail or in some cases were not previously known. For

these sources, their fluxes are generally high enough to allow sufficient counts in their spectra for more complex modeling. Thus, in this section, we investigate their X-ray behavior in more detail, and we attempt to determine their nature with some help from radio data provided by the MAVERIC survey (Shishkovsky et al. 2018; Tremou et al. 2018) and optical catalogs like the ACS treasury (Sarajedini et al. 2007).

We use a similar fitting process as in the catalog, taking spectra in the 0.3–10 keV band (binned to contain at least one background count per bin), fitting with XSPEC and BXA, and using model log-evidence ($\log_{10}Z$; Buchner et al. 2014) to identify the best model. Besides the power-law and APEC models used in the automated fitting in the catalog, we also tested an absorbed NS atmosphere model (NSATMOS in Xspec, with NS mass and radius fixed to $1.4 M_{\odot}$ and 10 km, respectively; McClintock et al. 2004; Heinke et al. 2006a). When feasible, we considered reasonable multicomponent models like NS atmosphere + power law, or double APEC. These choices allow for a range of physically motivated models, for example, spectra that might be dominated by the hot surface emission from the NS or a nonthermal accretion flow associated with an NS or BH (or combination thereof), or in the case of an accreting WD, a multitemperature hot plasma. The spectra and best-fit models for these sources are plotted in Figures 11 and 12, results of model comparisons are tabulated in Table 4, and best-fit values of parameters for each source are reported in Table 5. Figures 11 and 12 also include quantile–quantile (qq) plots (as produced by BXA) for the accumulated distribution of observed counts versus the expected distribution from the best-fit model (plotted on the left of each qq plot) to facilitate evaluation of any possible data or model excess.

CXOU J173538.12–303032.0 is a rather bright X-ray source in the field of Terzan 1 (2/5 away from cluster center) with a clear radio counterpart in the ATCA data from the MAVERIC survey (with a flux of $44 \pm 9 \mu\text{Jy}$ at 9 GHz and a $3 - \sigma$ upper limit of $47 \mu\text{Jy}$ at 5.5 GHz). The source shows little evidence of variation within the Chandra/ACIS observations. However, there is suggestive evidence for variability among the three observations covering Terzan 1 (K-S p -value of 0.01). The X-ray spectrum appears hard, best fit with an absorbed power law (Table 4). Regarding the nature of this source and its association with Terzan 1, it is important to consider that the cluster half-light radius as reported in the Harris catalog (3/8) is likely substantially overestimated (e.g., Cackett et al. 2006). We did perform the analysis in our catalog assuming the value from the Harris catalog as a conservative upper limit (as removing already-analyzed sources is considerably easier than adding new areas or sources to the analysis). However, when we consider the DSS infrared image of the cluster (Figure 1), the half-light radius is likely $\lesssim 1'$. In this case, CXOU J173538.12–303032.0 is probably unassociated with the cluster, but instead a likely background AGN, as the constraints on the N_{H} indicate the source is unlikely to be a foreground object.

CXOU J185502.95–302845.1 is the brightest source in M54. However, due to the large distance to the cluster (26.5 kpc), the source spectrum contains <100 counts, limiting our ability to study the source in detail. There is no evidence for variability of the source in the single Chandra/ACIS observation of this GC (K-S p -value of 0.65). Fitting the spectrum and comparing the models listed at the beginning of this section, we find that an absorbed NS

atmosphere fits the spectrum best (TBABS \times NSATMOS), with an absorbed NS atmosphere + power law slightly less likely (with relative probability of 53%; Table 4). These probabilities indicate that while an NS is highly likely as one of the members of the binary, there is weak evidence for the presence of a second component, such as power-law emission from weak accretion. We found no radio counterpart at the position of the X-ray source in the VLA data from the MAVERIC survey, with a 3σ upper limit of $<7.1 \mu\text{Jy}$ at a frequency of 6.1 GHz, equivalent to a radio limit of $<3 \times 10^{28} \text{ erg s}^{-1}$ at 5 GHz assuming a flat spectrum. This poor upper limit, due to the large distance of M54, is not very valuable.

CXOU J180801.98–434255.3 is the brightest X-ray source in NGC 6541. The source is bright enough that effects of pileup should be considered in spectral modeling. Thus, we performed a new set of spectral analyses, with the Chandra pileup model²⁴ (Davis 2001) added as a spectral component. We find that the spectrum is best fit with an absorbed NS atmosphere + power law (PILEUP \times TBABS \times [NSATMOS+PEGPWLW]), with an X-ray luminosity of $1.9_{-0.2}^{+0.3} \times 10^{33} \text{ erg s}^{-1}$ in the 0.5–10 keV band. The model fits the observed spectrum nicely with no significant trend in residuals (Figure 11, top panels). The power-law component is only loosely constrained, which sometimes suggests it may not be needed. However, comparing model log-evidence between this model and a single absorbed NSATMOS indicates the single-component model is 0.1% as likely as the two-component model (Table 4). We also find no significant evidence of variability in the single Chandra/ACIS observation covering this source. The best-fit X-ray spectral model suggests that this system is likely an NS-LMXB accreting at low levels. Inspecting the ATCA radio data from the MAVERIC survey (V. Tudor et al. 2020, in preparation), we found no detection of a radio source at the position of the X-ray source, with an average 3σ limit of $<11.7 \mu\text{Jy}$ at an average frequency of 7.25 GHz (Tremou et al. 2018). Assuming a flat radio spectrum and a cluster distance of 7.5 kpc (based on the Harris catalog), we find this flux density limit corresponds to a radio luminosity upper limit of $<3.9 \times 10^{27} \text{ erg s}^{-1}$ at the standard reference frequency of 5 GHz. This limit falls close to the radio luminosity observed for accreting BHs at these X-ray luminosities and perhaps slightly above that for transitional MSPs, so in this case the radio data do not strongly constrain the nature of the source.

CXOU J180449.72–073526.7 is the brightest X-ray source in NGC 6539, with $L_{\text{X}} \sim 2 \times 10^{33} \text{ erg s}^{-1}$. The source shows strong evidence for variability in a 15 ks Chandra/ACIS observation, with a K-S p -value of 3×10^{-7} . The source shows a hard X-ray spectrum, best fit by an absorbed power law or an absorbed APEC. An APEC model is 77% as likely as the power-law model, with NS + power law following with a 55% relative probability. Thus, while the presence of a hard power-law/APEC-like component is clear, we are unable to infer confidently whether a second (possibly softer) component is needed with the current data. The VLA radio catalog for this cluster from the MAVERIC survey (L. Shishkovsky et al. 2020, in preparation) shows a clear radio continuum counterpart to this X-ray source, with flux densities of 9.6 ± 1.9 and $12.7 \pm 2.4 \mu\text{Jy}$ at 5.2 and 7.2 GHz, respectively. These values imply a spectral index (for $S_{\nu} \sim \nu^{\alpha}$) of $\alpha = 0.51_{-0.76}^{+0.53}$, consistent with a flat or even inverted spectrum. Given the uncertainty in the spectral index, we assume that the 5 GHz flux

²⁴ <https://heasarc.gsfc.nasa.gov/docs/software/lheasoft/xanadu/xspec/manual/XSmodelPileup.html>

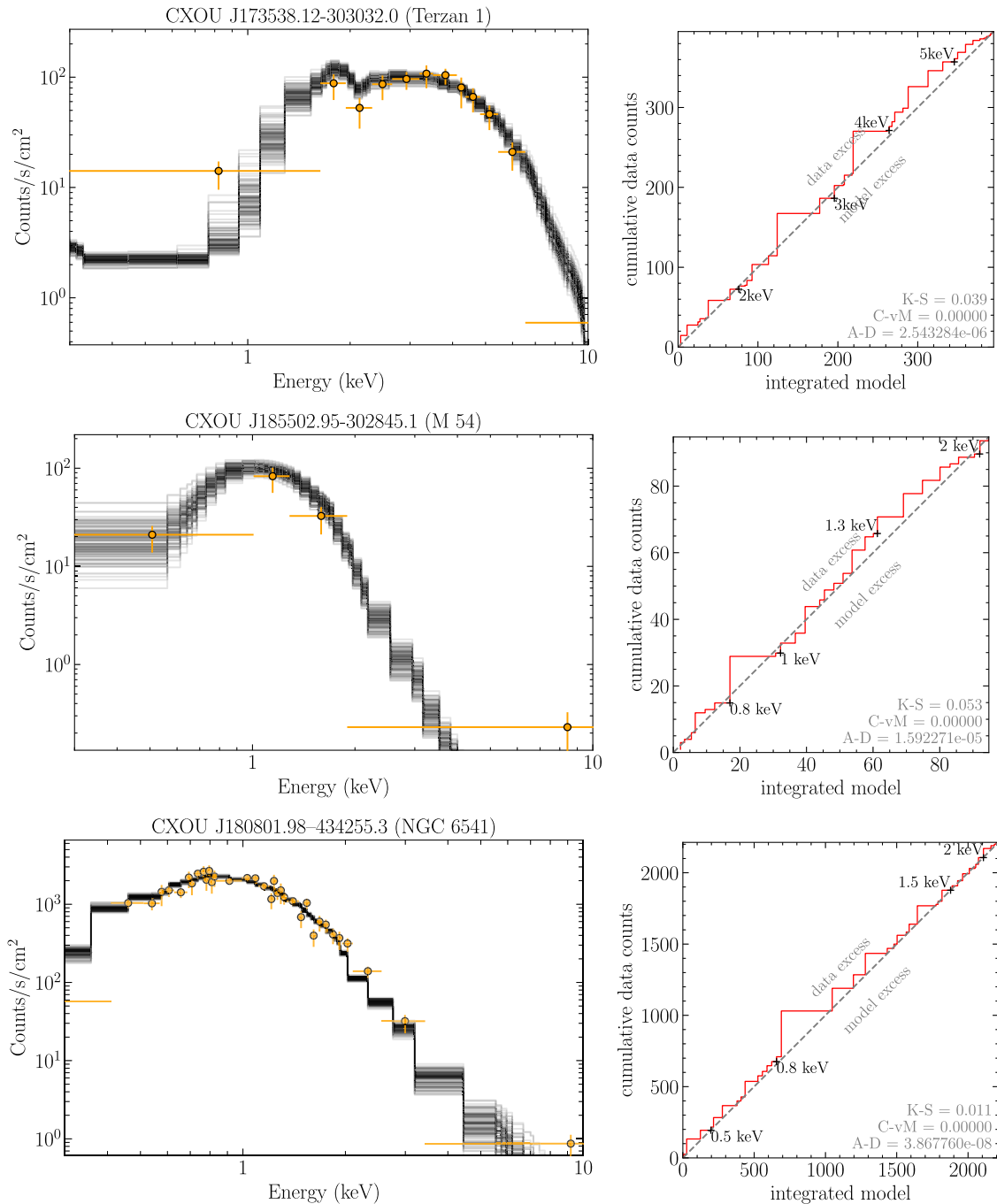


Figure 11. X-ray spectra (left) and quantile–quantile (qq) plot for the bright sources analyzed here. The black curves represent a random sample from the posterior distributions for the best-fit model in each case (Table 4). For the purpose of plotting, the data in the spectral plots have been binned adaptively with at least 20 counts. All qq plots are drawn in the 0.3–10.0 keV band (bottom left corner represents 0.3 keV, top right corner represents 10 keV), where the data were considered for spectral analysis.

density is best given by the 5.2 GHz value, corresponding to a luminosity of $3.5 \pm 0.7 \times 10^{27} \text{ erg s}^{-1}$. Plotting this source on the radio/X-ray correlation for known LMXBs (Figure 13) shows that it is in the region occupied both by BHs and by transitional MSPs in the subluminal disk state. There is mounting evidence that BHs, transitional MSPs, and accreting MSPs can occupy similar regions of this diagram at $L_X < 10^{35} \text{ erg s}^{-1}$ (e.g., Russell et al. 2018; Gusinskaia et al. 2020), and little is known about the radio behavior of typical NS-LMXBs in this regime. Hence, other interpretations of this

system are possible, and additional follow-up observations will be necessary to better understand this intriguing source.

CXOU J185503.47–302847.6 is the second-brightest X-ray source in M54. The morphology of the source in the image suggests that it may be confused/blended or extended (Figure 14). Unfortunately, due to the low number of counts (~ 40 in the 0.5–10 keV band), it is difficult to disentangle confidently. Assuming it is a single point source, the source spectrum is best fit by an absorbed APEC model. An absorbed power-law or power-law + NS atmosphere are also likely

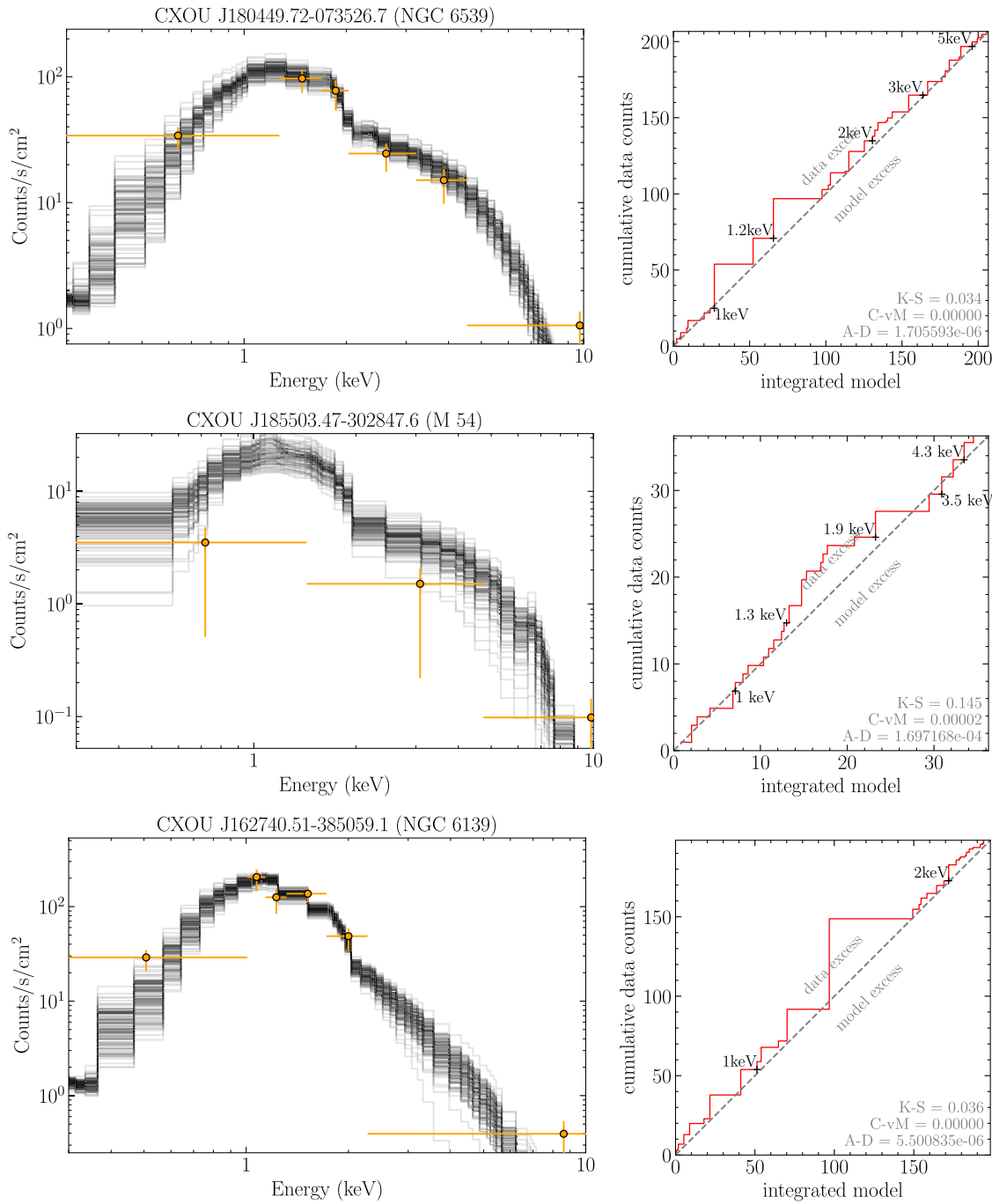


Figure 12. Similar to Figure 11. X-ray spectra (left) and qq plot for the bright sources analyzed here. The black curves represent a random sample from the posterior for the best-fit model in each case (Table 4). For the purpose of plotting, the data in the spectral plots have been binned adaptively with at least 20 counts (five counts in the case of CXOU J185503.47–302847.6). All qq plots are drawn in the 0.3–10.0 keV band (bottom left corner represents 0.3 keV, top right corner represents 10 keV), where the data were considered for spectral analysis.

models, with probabilities of 15%–30% (relative to APEC). It is difficult to assess the possible nature of this source, due to the possible source confusion and low counts, but the spectrum is consistent with some LMXBs and bright CVs. Similar to CXOU J185502.95–302845.1 (the brightest source in M54), this source had no radio counterpart to a comparable limit.

Lastly, CXOU J162740.51–385059.1 is the brightest source in NGC 6139. This source was previously identified in ROSAT data (Verbunt 2001), but it remains poorly studied. The source shows no significant evidence of variability in the single Chandra/ACIS observation of this GC (with a K-S p -value of

0.5, indicating no evidence of variability in the current data²⁵). The source clearly shows a rather soft spectrum, best fit by an absorbed NS atmosphere + power law (TBABS \times [NSATMOS+PEGPWRLW]), with an X-ray luminosity of $1.1^{+0.5}_{-0.2} \times 10^{33}$ erg s⁻¹ in the 0.5–10 keV band. It is worth noting that the absorbed power law also shows a high relative likelihood and is not entirely ruled out as a possible model (Table 4). These models indicate that the system is probably another weakly

²⁵ Values closer to zero indicate stronger evidence for variability.

Table 4
Model Comparison for the Sample of Bright Sources Analyzed in This Work

CXOU J	GC	$\log_{10}Z$				
		AP	$2 \times$ AP	PL	NS	NS + PL
173538.12–303032.0	Terzan 1	−0.58	−9.56	0.00	−54.70	−0.11
185502.95–302845.1	M54	−2.81	−6.50	−1.17	0.00	−0.27
180801.98–434255.3	NGC 6541	−63.37	−31.35	−2.81	−2.80	0.00
180449.72–073526.7	NGC 6539	−0.11	−25.03	0.00	−52.26	−0.26
185503.47–302847.6	M54	0.00	−14.48	−0.53	−9.70	−0.37
162740.51–385059.1	NGC 6139	−2.48	−8.29	−0.20	−1.92	0.00

Note. We used model evidence ($\log_{10}Z$) as implemented in BXA, normalized to the model with the highest evidence in each case. In this representation, the evidence indicates the relative likelihood of the models. Models tested here are APEC (AP), power law (PL), neutron star atmosphere (NS), and reasonable combinations of them. Values in bold represent the most likely models.

Table 5
Best-fit Values of Parameters and Uncertainties Based on Posterior Distributions (Median and 90% Credible Intervals) for the Most Likely Models

CXOU J	GC	Model	N_{H} (10^{21} cm^{-2})	kT (keV)	Γ	Unabs. Flux ($10^{-14} \text{ erg s}^{-1} \text{ cm}^{-2}$)	$\log_{10}(A-D)$
173538.12–303032.0	Terzan 1	PL	35^{+8}_{-7}	...	1.2 ± 0.3	39^{+5}_{-3}	−5.6
185502.95–302845.1	M54	NS	2 ± 1	0.14 ± 0.006	...	$2.4^{+1.5}_{-0.4}$	−4.8
180801.98–434255.3	NGC 6541	NS + PL	$1.8^{+1.5}_{-0.4}$	$0.133^{+0.003}_{-0.006}$	$2.9^{+1.0}_{-2.2}$	29^{+6}_{-3}	−7.4
180449.72–073526.7	NGC 6539	PL	5 ± 2	...	1.6 ± 0.3	21 ± 3	−5.8
185503.47–302847.6	M54	AP	< 1.4	11^{+13}_{-6}	...	1.7 ± 0.4	−3.8
162740.51–385059.1	NGC 6139	NS + PL	9^{+3}_{-2}	0.08 ± 0.05	$3.8^{+0.6}_{-1.3}$	9^{+4}_{-2}	−5.3

Note. kT represents the temperature (neutron star atmosphere, or hot plasma in APEC). Γ is the power-law photon index. Flux values are unabsorbed in the 0.5–10 keV band. $\log_{10}(A-D)$ represents the Anderson–Darling statistics value (not p -values). Smaller values indicate a better fit.

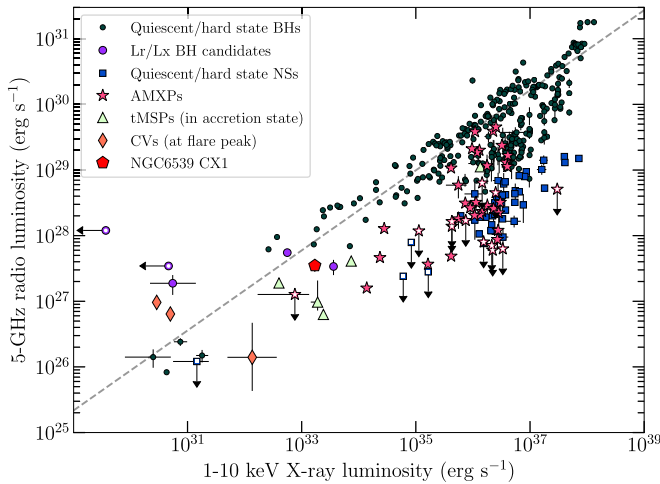


Figure 13. Radio/X-ray correlation for accreting compact objects, showing NGC 6539 CX1 (CXOU J162740.51–385059.1) consistent with accreting black holes and tMSPs. However, we note that some accreting neutron stars and accreting millisecond X-ray pulsars may show radio luminosities similar to black holes with similar X-ray luminosity (Russell et al. 2018; Gusinskaia et al. 2020). The dark green circles show known black holes in the Galactic field (e.g., Miller et al. 2011; Gallo et al. 2012; Corbel et al. 2013; Plotkin et al. 2017). The dashed grey line shows the best-fit correlation for black holes from Gallo et al. (2014). Purple circles show radio-selected black hole candidates (Strader et al. 2012; Chomiuk et al. 2013; Miller-Jones et al. 2015; Tetarenko et al. 2016; Bahramian et al. 2017). Light green triangles show tMSPs (Papitto et al. 2013; Deller et al. 2015; Bogdanov et al. 2018). Blue squares and pink stars are accreting neutron stars (in the hard state) and accreting millisecond X-ray pulsars (Migliari & Fender 2006; Tudor et al. 2017). Orange diamonds are bright CVs and the pulsating white dwarf AR Sco (Marsh et al. 2016; Russell et al. 2016). The plot is from Bahramian et al. (2018).

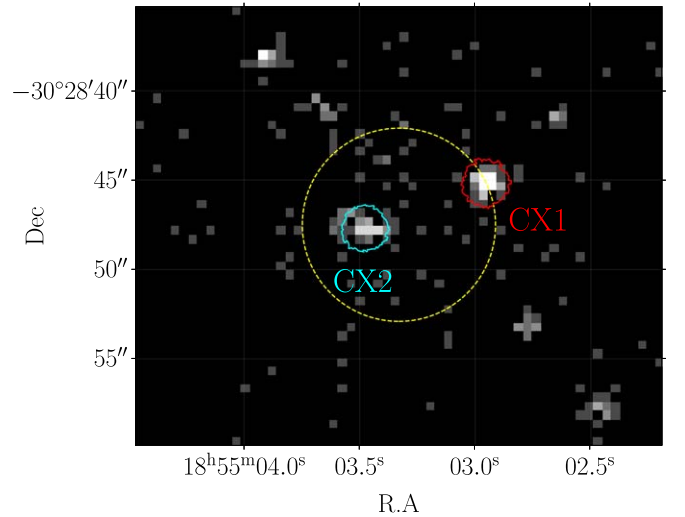


Figure 14. Core of M54 (dashed yellow circle) as seen by Chandra/ACIS. The cluster contains two X-ray sources with $L_{\text{X}} > 10^{33} \text{ erg s}^{-1}$ as discussed in the text: M54 CX1 (CXOU J185502.95–302845.1) and M54 CX2 (CXOU J185503.47–302847.6), denoted by red and cyan regions, respectively. The morphology of the M54 CX2 in the image suggests that it may be confused/blended or extended.

accreting NS-LMXB. Considering the ATCA radio data for this source, we again found no evidence of radio emission, with a 3σ upper limit of $< 10.8 \mu\text{Jy}$ at 7.25 GHz. Again assuming a flat spectrum, we find this corresponds to a reference 5 GHz radio luminosity upper limit of $< 6.6 \times 10^{27} \text{ erg s}^{-1}$ at a distance of 10.1 kpc. As for the previous source, this limit does

not substantially constrain the nature or state of the accreting compact object.

5.4. Populations of Moderately Bright X-Ray Sources

We can use the results from our survey of bright X-ray sources in 38 GCs to place interesting constraints on several X-ray source populations.

5.4.1. Intermediate Polars

First, we discuss X-ray-bright intermediate polars (IPs). Intermediate polars are unusual among CVs in being highly efficient at converting accretion energy into X-rays even at high accretion rates, unlike disk-accreting CVs (Patterson & Raymond 1985; Patterson 1994). Pretorius & Mukai (2014) showed that there are two populations of IPs: an X-ray-bright sample and a low-luminosity sample. With Gaia distances, it has become clear that the bright IPs generally have X-ray luminosities of 10^{33} to 2×10^{34} erg s⁻¹ (Suleimanov et al. 2019; Schwöpe 2018), while the fainter IP population, mostly shorter-period systems below the period gap, have L_X between 10^{30} and 10^{32} erg s⁻¹. Many bright IPs have been detected in the Galactic Field with all-sky hard X-ray coded-mask surveys (*INTEGRAL* and Swift/BAT; Barlow et al. 2006; Baumgartner et al. 2013). Of particular importance is that the same bright IP systems that can be surveyed over the whole sky are also all bright enough to appear in our $L_X > 10^{33}$ erg s⁻¹ sample.

Pretorius & Mukai (2014) carefully estimated the space density of X-ray-bright IPs using the Swift/BAT survey, finding a local space density of $1_{-0.5}^{+1} \times 10^{-7}$ pc⁻³ (much of the uncertainty comes from the uncertain disk scale height of the IP population). Schwöpe (2018) used Gaia DR2 distances to update the space density to $7.4_{-1.7}^{+4.8} \times 10^{-8}$ pc⁻³. For a local stellar density of 0.1 stars pc⁻³ (Gliese & Jahreiß 1991), that equates to 7×10^{-7} bright IPs per star, or (assuming an average stellar mass of $0.5 M_\odot$) $1.5_{-0.3}^{+1.0} \times 10^{-6}$ bright IPs per M_\odot .

We sum the masses of the 38 GCs in our sample using the calculations of Baumgardt & Hilker (2018),²⁶ giving a total mass of $1.37 \times 10^7 M_\odot$, for a predicted number of 21_{-5}^{+13} bright IPs in these GCs, assuming the field rate of IPs per stellar mass.

However, we see only two (maybe three) plausible IP candidates among our moderately bright GC X-ray sources. This is a factor of 10 fewer IPs than expected, at more than 3σ significance. Intriguingly, this is the opposite result from Grindlay et al. (1995), who suggested an overabundance of magnetic CVs in GCs; several papers have since attempted to explain this overabundance (e.g., Dobrotka et al. 2006; Ivanova et al. 2006).

It is not obvious how to explain the opposite result of fewer IPs in GCs. The destruction of the wide binaries that are CV progenitors (pre-common envelope) in the dense environments of GCs is a logical direction. However, the reduction of CV numbers in GCs has been estimated at only a factor of 2–3 (Shara & Hurley 2006; Haggard et al. 2009), and CV numbers are higher in denser GCs (e.g., Pooley et al. 2003; Heinke et al. 2020). D. Belloni et al. (2020, in preparation) will discuss possible solutions to this problem.

5.4.2. Symbiotic Stars

We have no good candidate symbiotic stars in our $L_X > 10^{33}$ erg s⁻¹ sample. In the field, symbiotic stars with $L_X \sim 10^{33}$ erg s⁻¹ but without strong optical emission lines (suggesting an accretion luminosity below $\sim 10^{34}$ erg s⁻¹; Mukai et al. 2016) appear to be somewhat common (van den Berg et al. 2006; Hynes et al. 2014; Mukai et al. 2016), though not well studied. Lü et al. (2006) estimate 1200–15,000 symbiotic stars in the galaxy with accretion luminosity above $10 L_\odot$. Systems with lower accretion rates (as in Mukai et al. 2016) should be more numerous. Munari & Renzini (1992) empirically estimate 3×10^5 symbiotic stars in the galaxy, but a theoretical prediction of the number of symbiotics with lower accretion luminosities would be of great interest.

If we take 3×10^5 symbiotic stars in our Galaxy (assumed $10^{11} M_\odot$), we can estimate that ~ 40 symbiotic stars should be present in our GC sample. However, their luminosity function is unknown. If we make the (doubtful) assumptions that van den Berg et al. (2006) detected all of the symbiotics in their Galactic Bulge FOV, that they are all symbiotics, and that those systems are all located at 8 kpc, then we may infer that 1/13 symbiotic stars have $L_X \sim 10^{33}$ erg s⁻¹. This would suggest about three symbiotic stars in our sample. The lack of symbiotic stars (if the assumptions above prove reasonable) should not be surprising, however, due to the destruction of wide binaries in GCs (e.g., Belloni et al. 2020).

There have been suggestions of symbiotic stars in some GCs. Henleywillis et al. (2018) identified a symbiotic star in ω Cen, through a robust identification of an $L_X \sim 3 \times 10^{32}$ erg s⁻¹ X-ray source with a red giant (a carbon star). Belloni et al. (2020) suggest that the symbiotic star in ω Cen has been misclassified, as they do not see an optical H α emission line in their SALT spectrum. A requirement of strong optical H emission lines has often been used to confirm symbiotic stars (see, e.g., Allen 1984; Belczyński et al. 2000). However, a number of symbiotic systems have been suggested based on other wavelengths, such as X-ray emission, without H emission lines (Hynes et al. 2014; Bahramian et al. 2014). Mukai et al. (2016) confidently identify SU Lynx as a WD accreting from a red giant, though it shows only weak H lines. Munari (2019) shows that even weak H emission lines are not always present in high-resolution spectra of SU Lynx (see also Kenyon & Garcia 2016 for the occasional absence of H emission lines in EG And) and proposes an alternative definition of symbiotic stars in which any binary where a WD or NS accretes enough material from an RG to be detected at any wavelength is considered a symbiotic binary. Thus, careful multiwavelength observations are needed for accurate classification of symbiotic systems.

5.4.3. Transitional Millisecond Pulsars

We can also constrain the numbers of tMSPs in their “active” state (with $L_X \sim 10^{33} - 10^{34}$ erg s⁻¹). Note that it is currently unclear whether the “active” state represents active, low-level accretion onto the NS (e.g., Jaodand et al. 2016) or enhanced radio pulsar emission (Ambrosino et al. 2017).

We have one to two “active” tMSP candidates among our 38 clusters (IGR J18245–2452 and perhaps Ter5 CX1; Bahramian et al. 2018). We can roughly estimate the total number of qLMXBs in these clusters by adding up the calculated stellar interaction rates for these clusters (tabulated in Bahramian et al. 2013), which amount to 40% of the total stellar interaction rate of

²⁶ <https://people.smp.uq.edu.au/HolgerBaumgardt/globular/parameter.html>

the Milky Way’s GC system. Estimating 250 qLMXBs in the entire GC system (extrapolating from the five qLMXBs in 47 Tuc; Heinke et al. 2005a, 2005b) implies ~ 100 quiescent LMXBs among these clusters.

From these numbers, we can conclude that the average quiescent LMXB spends only $\sim 2\%$ of its lifetime in a transitional MSP “active” state. Of course, we do not know what fraction of LMXBs pass through a transitional MSP phase, or for how long, nor do we know what fraction of the transitional MSP phase these systems spend in their “active” state; our analysis cannot separate these questions.

A caveat is that we will miss tMSPs in the “active” state if we only use stacked data in which a tMSP is only “active” for a short time. For instance, Ter5 CX1 was rarely X-ray bright, so its averaged L_X in the stacked image falls below 10^{33} erg s $^{-1}$. However, only three of our clusters were observed at more than two epochs, suggesting that we have probably found the “active” tMSPs in our sample. Note that the two tMSPs we have found were in the three clusters observed the most, suggesting that a number of tMSPs may be hidden in our clusters (e.g., 47 Tuc V; Ridolfi et al. 2016).

6. Conclusion

In this paper, we provide a deep and extended catalog of faint ($L_X < 10^{35}$ erg s $^{-1}$) X-ray sources in a sample of 38 Galactic GCs. We perform photometry, variability, and spectral analysis for each of more than 1100 sources, and we catalog the results of these analyses. We also investigate the X-ray properties, the nature and population of faint XRBs in GCs, and their luminosity function, which is now the deepest X-ray luminosity function of GC XRBs.

The X-ray sources reviewed in Section 5.3.1 and the new ones identified in Section 5.3.2 provide us with a large (and fairly complete) sample of XRBs with $10^{33} \leq L_X \leq 10^{35}$ erg s $^{-1}$ in this set of Galactic GCs. This sample allows us to explore the population of weakly accreting systems in GCs. While such sources in the field are heterogeneous, containing BH-LMXBs and NS-LMXBs, transitional MSPs, CVs, and symbiotic X-ray binaries (e.g., Shaw et al. 2020), the GC sample here seems somewhat less diverse, with a large population of NS-LMXBs, two CV candidates, and a BH-LMXB/tMSP candidate.

Besides the systems reviewed and identified in this work with $10^{33} \leq L_X \leq 10^{35}$ erg s $^{-1}$, there are three other GC LMXBs identified in Galactic GCs with similar luminosities: the BH-LMXB candidate 47 Tuc X9 (Miller-Jones et al. 2015; Bahramian et al. 2017), the candidate NS-LMXB M15 X-3 (Heinke et al. 2009; Arnason et al. 2015), and the unusual variable source NGC 6652B (Stacey et al. 2012; these GCs were not in our current paper; see Section 2.1). It is worth noting that this sample is not complete. It is possible for some sources in our survey that show $L_X < 10^{33}$ erg s $^{-1}$ to have heavy partial covering or intrinsic absorption, and thus for their true luminosity to be substantially higher. There are also likely to be similar systems in GCs not covered in our survey or in other studies. In the $L_X > 10^{35}$ erg s $^{-1}$ regime, out of 21 transient and persistent systems identified in Galactic GCs so far, 20 are confirmed or candidate NS-LMXBs, with one of them a confirmed tMSP (IGR J18245-2452, Papitto et al. 2013). The only exception so far has been the transient source 1E 1339.8+2837 in M3, which appears to be an accreting WD that showed an episode of (somewhat underluminous) supersoft

X-ray emission (Grindlay 1993; Verbunt et al. 1995; Edmonds et al. 2004). In the 10^{33} – 10^{35} erg s $^{-1}$ range, while NS-LMXBs appear to still hold a majority, the contributions from other classes of objects become noticeable. Out of 15 systems identified so far (12 reviewed or identified in this study, plus the three systems mentioned above), 10 are candidate or confirmed NS-LMXBs (with one plausible tMSP candidate), two are candidate BH-LMXBs, two are candidate CVs, and one is an unusually X-ray bright pulsar. The classification of numerous, fainter sources with $L_X < 10^{33}$ erg s $^{-1}$ will be an essential focus of future work.

Lastly, we inspected the populations of classes of bright 10^{33} – 10^{35} erg s $^{-1}$ sources in our sample. We noticed a significant deficit of bright ($L_X > 10^{33}$ erg s $^{-1}$) intermediate polar CVs in GCs, compared to their abundance in the field. This is intriguing, as GCs have long been thought to be *overabundant* in magnetic CVs, particularly intermediate polars. We find (more speculative) evidence for an underabundance of symbiotics in GCs, which is not surprising considering their likelihood of disruption by encounters, due to their large orbits. We also show that quiescent LMXBs in GCs may spend $\sim 2\%$ of their lifetimes in a transitional MSP “active” state, with $L_X \sim 10^{33}$ – 10^{34} erg s $^{-1}$ (we do not constrain their lifetimes in the lower- L_X “passive” transitional MSP state).

We thank the anonymous referee for their helpful comments. A.B. thanks Patrick Broos, Diogo Belloni, Lilianna Rivera Sandoval, and Scott Ransom for helpful discussions. J.C.A.M.J. is the recipient of an Australian Research Council Future Fellowship (FT140101082) funded by the Australian government. L.C. is grateful for the support of NASA grants Chandra-G06-17040X, Chandra-GO7-18032A, and HST-GO-14351. J.S. acknowledges support from a Packard Fellowship, NASA grants Chandra-GO3-14029X, Chandra-GO5-16036X, and Chandra-GO8-19122X, and NSF grants AST-1308124 and AST-1514763. C.O.H. and G.R.S. acknowledge NSERC Discovery Grants RGPIN-2016-04602 and RGPIN-2016-06569, respectively, and C.O.H. also a Discovery Accelerator Supplement. K.L.L. is supported by the Ministry of Science and Technology of the Republic of China (Taiwan) through grant 108-2112-M-007-025-MY3. We acknowledge extensive use of NASA’s Astrophysics Data System Bibliographic Services, Arxiv, and SIMBAD (Wenger et al. 2000).

Facilities: Chandra (ACIS), VLA, ATCA.

Software: ACIS-Extract (Broos et al. 2010), Astropy (Astropy Collaboration et al. 2013, 2018), BXA (Buchner et al. 2014), CIAO (Fruscione et al. 2006), Corner (Foreman-Mackey 2016), HEASOFT (NASA High Energy Astrophysics Science Archive Research Center 2014), IPython (Perez & Granger 2007), Jupyter (Kluyver et al. 2016), Matplotlib (Hunter 2007), MultiNest (Feroz et al. 2019), Numpy (Oliphant 2006; van der Walt et al. 2011) Pwddetect (Damiani et al. 1997), SAOImage DS9 (Joye & Mandel 2003), Scipy (Virtanen et al. 2020), XSPEC (Arnaud 1996).

Appendix Overview of Catalog Columns

The final published catalog online contains 123 columns, including details of source coverage and properties. These detailed data are provided to allow careful further analysis by readers. The catalog in its complete form is available in the electronic version of this article. Here, in Table A1, we provide a detailed description of all of the columns in the catalog.

Table A1
Detailed Description of All of the Columns in the Final X-Ray Source Catalog Presented in This Work

Column name	Column Description
CXOU_J	Source designation following the Chandra convention for naming unregistered sources.
detection_quality_flag	If a source has a minimum false probability value of $\geq 1\%$, we classify it as a poor detection (with a detection quality flag value of 2). If a source has a minimum false probability value of $< 1\%$ and a net source count < 5 (in the 0.5–10 keV band), we classify it as a marginal detection (detection quality flag value = 1). Finally, if a source has a minimum false probability value of $< 1\%$ and a net source count ≥ 5 , we classify it as a confident detection (detection quality flag value = 0). For more details, see Section 4.2 and Figure 3.
spectrum_quality_flag	Indicates spectrum quality based on total number of source counts: if a source has ≥ 100 counts, it would have a relatively reliable spectral analysis (and we assign a flag value of 0). If the total number of counts is somewhere between $\lesssim 100$ and $\gtrsim 20$, the estimates are less reliable and should be taken with caution (flag value of 1). Lastly, if a source has $\lesssim 20$ counts, spectral analysis is merely suggestive, and model comparison is not to be taken with confidence (flag value of 2).
pile_up_flag	Whether the source is in danger of being piled up. If True, the photometry and spectroscopy presented in this catalog are likely inaccurate. Only 15 sources are identified as potentially piled up in our catalog.
foreground_flag	True means that the source could be a foreground object. This is determined based on comparing the upper limit on the source N_H (from the best-fit model) to the host cluster N_H (estimated based on $E(B - V)$). False does not necessarily reject that the source is a foreground object, just that the source N_H is not inconsistent with the host cluster. Refer to Sections 4.7 and 5.1 for details on this assessment and its caveats.
Prob_AGN	Probability that the source may be a background AGN. Estimated based on source flux, population of sources in the cluster, and the location of the source in the cluster. If the source is located outside the GC half-light radius, this probability is not estimated. See Section 4.7 for details.
abs_astrometry_flag	If the coordinates are corrected for absolute astrometry. This is currently only done for Terzan 5. For the rest of the catalog, one should consider an additional $0.8''$ uncertainty to consider Chandra's astrometry accuracy.
R.A._centroid	Source R.A. estimated via centroiding (coordinates used for most analyses in this paper).
Decl._centroid	Source decl. estimated via centroiding (coordinates used for most analyses in this paper).
Centroid_error	Centroiding uncertainty radius (arcsec).
R.A._recon	Source R.A. estimated via image reconstruction.
Decl._recon	Source decl. estimated via image reconstruction.
R.A._correlate	Source R.A. estimated via correlating image and PSF.
Decl._correlate	Source decl. estimated via correlating image and PSF.
Num_obs_total	Total number of observations covering the source.
Num_obs_merged	Number of observations merged for this source to enhance source validity.
Exposure	Total source-specific exposure time from the merged observations (s).
Primary_ccd	The Chandra/ACIS CCD (ACIS-I or ACIS-S) that contains most or all of the observations covering the source.
theta_avg	Average off-axis angle (arcmin).
theta_low	Minimum off-axis angle (arcmin).
theta_high	Maximum off-axis angle (arcmin).
psf_fraction	Average PSF fraction.
src_cnts_*	Total source counts in different bands.
bkg_cnts_*	Total background counts in different bands.
backscale_*	Background scaling factor in different bands.
net_cnts_*	Net source counts in different bands.
net_cnts_sigma_up_*	1σ upper limit on net source counts in different bands.
net_cnts_sigma_low_*	1σ lower limit on net source counts in different bands.
significance_*	Photometric signal-to-noise ratio in different bands.
prob_no_source_*	p -value for no-source hypothesis in different bands.
min_KS_single_obs	Minimum p -value for K-S variability test within each observation. These values should be considered with caution. See Sections 4.5 and 5.1 for further details.
KS_all_data	p -value for K-S variability test for all observations. These values should be considered with caution. See Sections 4.5 and 5.1 for further details.
ae_abs_flux_*kev	Absorbed flux in different bands based on a power-law fit in AE ($\text{erg s}^{-1} \text{cm}^{-2}$).
ae_unabs_flux_*kev	Unabsorbed flux in different bands based on a power-law fit in AE ($\text{erg s}^{-1} \text{cm}^{-2}$).
fit1_pl_nh	BXA Power-law fit N_H (cm^{-2}).
fit1_pl_nh_er-	BXA Power-law fit lower uncertainty (cm^{-2}).
fit1_pl_nh_er+	BXA Power-law fit upper uncertainty (cm^{-2}).
fit1_pl_gamma	BXA Power-law fit photon index.
fit1_pl_gamma_er-	BXA Power-law fit photon index lower uncertainty.
fit1_pl_gamma_er+	BXA Power-law fit photon index upper uncertainty.
fit1_pl_flux_0.5-10	BXA Power-law fit unabsorbed flux in the 0.5–10 keV band ($\text{erg s}^{-1} \text{cm}^{-2}$).
fit1_pl_flux_0.5-10_er-	BXA Power-law fit unabsorbed flux lower uncertainty in the 0.5–10 keV band ($\text{erg s}^{-1} \text{cm}^{-2}$).
fit1_pl_flux_0.5-10_er+	BXA Power-law fit unabsorbed flux upper uncertainty in the 0.5–10 keV band ($\text{erg s}^{-1} \text{cm}^{-2}$).
fit1_pl_lum_0.5-10	BXA Power-law fit luminosity in the 0.5–10 keV band (assuming cluster distance; erg s^{-1}).
fit1_pl_lum_0.5-10_er-	BXA Power-law fit luminosity lower uncertainty in the 0.5–10 keV band (erg s^{-1}).
fit1_pl_lum_0.5-10_er+	BXA Power-law fit luminosity upper uncertainty in the 0.5–10 keV band (erg s^{-1}).
fit1_pl_logrelprob	\log_{10} of goodness probability of the power-law model (normalized relative to the best model, which will have a probability of 1).

Table A1
(Continued)

Column name	Column Description
fit2_apec_nh	APEC fit N_{H} (cm^{-2}).
fit2_apec_nh_er-	BXA APEC fit lower uncertainty (cm^{-2}).
fit2_apec_nh_er+	BXA APEC fit upper uncertainty (cm^{-2}).
fit2_apec_kT	BXA APEC temperature (keV).
fit2_apec_kT_er-	BXA APEC temperature lower uncertainty (keV).
fit2_apec_kT_er+	BXA APEC temperature upper uncertainty (keV).
fit2_apec_flux_0.5-10	BXA APEC fit unabsorbed flux in the 0.5–10 keV band ($\text{erg s}^{-1} \text{cm}^{-2}$).
fit2_apec_flux_0.5-10_er-	BXA APEC fit unabsorbed flux lower uncertainty in the 0.5–10 keV band ($\text{erg s}^{-1} \text{cm}^{-2}$).
fit2_apec_flux_0.5-10_er+	BXA APEC fit unabsorbed flux upper uncertainty in the 0.5–10 keV band ($\text{erg s}^{-1} \text{cm}^{-2}$).
fit2_apec_lum_0.5-10	BXA APEC fit luminosity in the 0.5–10 keV band (assuming cluster distance; erg s^{-1}).
fit2_apec_lum_0.5-10_er-	BXA APEC fit luminosity lower uncertainty in the 0.5–10 keV band (erg s^{-1}).
fit2_apec_lum_0.5-10_er+	BXA APEC fit luminosity upper uncertainty in the 0.5–10 keV band (erg s^{-1}).
fit2_apec_logrelprob	\log_{10} of goodness probability of the APEC model (normalized relative to the best model, which will have a probability of 1).
fit3_bbbodyrad_nh	BXA Blackbody fit N_{H} (cm^{-2}).
fit3_bbbodyrad_nh_er-	BXA Blackbody fit lower uncertainty (cm^{-2}).
fit3_bbbodyrad_nh_er+	BXA Blackbody fit upper uncertainty (cm^{-2}).
fit3_bbbodyrad_kT	BXA Blackbody temperature (keV).
fit3_bbbodyrad_kT_er-	BXA Blackbody temperature lower uncertainty (keV).
fit3_bbbodyrad_kT_er+	BXA Blackbody temperature upper uncertainty (keV).
fit3_bbbodyrad_flux_0.5-10	BXA Blackbody fit unabsorbed flux in the 0.5–10 keV band ($\text{erg s}^{-1} \text{cm}^{-2}$).
fit3_bbbodyrad_flux_0.5-10_er-	BXA Blackbody fit unabsorbed flux lower uncertainty in the 0.5–10 keV band ($\text{erg s}^{-1} \text{cm}^{-2}$).
fit3_bbbodyrad_flux_0.5-10_er+	BXA Blackbody fit unabsorbed flux upper uncertainty in the 0.5–10 keV band ($\text{erg s}^{-1} \text{cm}^{-2}$).
fit3_bbbodyrad_lum_0.5-10	BXA Blackbody fit luminosity in the 0.5–10 keV band (assuming cluster distance; erg s^{-1}).
fit3_bbbodyrad_lum_0.5-10_er-	BXA Blackbody fit luminosity lower uncertainty in the 0.5–10 keV band (erg s^{-1}).
fit3_bbbodyrad_lum_0.5-10_er+	BXA Blackbody fit luminosity upper uncertainty in the 0.5–10 keV band (erg s^{-1}).
fit3_bbbodyrad_logrelprob	\log_{10} of goodness probability of the blackbody model (normalized relative to the best model, which will have a probability of 1).
best_fit	Model with highest probability.
N_bg_agn_soft	Number of expected bkg sources with flux higher than the source in 0.5–2 keV, within the half-light radius of the GC based on Mateos et al. (2008).
N_bg_agn_hard	Number of expected bkg sources with flux higher than the source in 2–10 keV, within the half-light radius of the GC based on Mateos et al. (2008).
dist_from_gc_center	Source distance from the cluster center (arcmin).
gc_name	Host GC name
gc_distance	GC distance (kpc)
gc_nh	Host cluster N_{H} (cm^{-2}) as estimated based on cluster E(B–V). This value is not used in spectral analyses in this work and is provided for comparison.
gc_nh_er	Uncertainty in the host cluster N_{H} (cm^{-2}), considering the reported uncertainties on $E(B - V)$ in the Harris catalog, the reported uncertainty on the correlation slope by Bahramian et al. (2015), and assuming an uncertainty of 0.1 on R_V .
gc_cr_rad	Host cluster core radius (arcmin).
gc_hl_rad	Host cluster half-light radius (arcmin).

(This table is available in its entirety in machine-readable form.)

ORCID iDs

Arash Bahramian  <https://orcid.org/0000-0003-2506-6041>
Jay Strader  <https://orcid.org/0000-0002-1468-9668>
James C. A. Miller-Jones  <https://orcid.org/0000-0003-3124-2814>
Laura Chomiuk  <https://orcid.org/0000-0002-8400-3705>
Craig O. Heinke  <https://orcid.org/0000-0003-3944-6109>
Thomas J. Maccarone  <https://orcid.org/0000-0003-0976-4755>
David Pooley  <https://orcid.org/0000-0003-4897-7833>
Laura Shishkovsky  <https://orcid.org/0000-0003-0286-7858>
Vlad Tudor  <https://orcid.org/0000-0003-4553-4607>
Yue Zhao  <https://orcid.org/0000-0002-9547-8677>
Kwan Lok Li  <https://orcid.org/0000-0002-0439-7047>
Gregory R. Sivakoff  <https://orcid.org/0000-0001-6682-916X>
Evangelia Tremou  <https://orcid.org/0000-0002-4039-6703>
Johannes Buchner  <https://orcid.org/0000-0003-0426-6634>

References

- Allen, D. A. 1984, *PASAu*, 5, 369
Alpar, M. A., Cheng, A. F., Ruderman, M. A., & Shaham, J. 1982, *Natur*, 300, 728
Altamirano, D., Wijnands, R., Heinke, C. O., Sivakoff, G. R., & Pooley, D. 2012, *ATel*, 4264, 1
Ambrosino, F., Papitto, A., Stella, L., et al. 2017, *NatAs*, 1, 854
Archibald, A. M., Stairs, I. H., Ransom, S. M., et al. 2009, *Sci*, 324, 1411
Arnason, R. M., Sivakoff, G. R., Heinke, C. O., Cohn, H. N., & Lugger, P. M. 2015, *ApJ*, 807, 52
Arnaud, K. A. 1996, in *ASP Conf. Ser. 101: Astronomical Data Analysis Software and Systems V*, ed. G. H. Jacoby & J. Barnes (San Francisco, CA: ASP), 17
Astropy Collaboration, Price-Whelan, A. M., Sipőcz, B. M., et al. 2018, *AJ*, 156, 123
Astropy Collaboration, Robitaille, T. P., Tollerud, E. J., et al. 2013, *A&A*, 558, A33
Babu, G., & Rao, C. 2004, *The Indian Journal of Statistics*, 66, 63
Babu, G. J., & Feigelson, E. D. 2006, in *ASP Conf. Ser. 351, Astrostatistics: Goodness-of-Fit and All That!*, ed. C. Gabriel et al. (San Francisco, CA: ASP), 127

- Bagchi, M., Lorimer, D. R., & Chennamangalam, J. 2011, *MNRAS*, **418**, 477
- Bahramian, A., Heinke, C. O., Degenaar, N., et al. 2015, *MNRAS*, **452**, 3475
- Bahramian, A., Heinke, C. O., Sivakoff, G. R., et al. 2014, *ApJ*, **780**, 127
- Bahramian, A., Heinke, C. O., Sivakoff, G. R., & Gladstone, J. C. 2013, *ApJ*, **766**, 136
- Bahramian, A., Heinke, C. O., Tudor, V., et al. 2017, *MNRAS*, **467**, 2199
- Bahramian, A., Kennea, J. A., Heinke, C. O., et al. 2019, *ATel*, **13192**, 1
- Bahramian, A., Miller-Jones, J., Strader, J., et al. 2018, Radio/X-ray Correlation Database for X-ray Binaries, v0.1, Zenodo, doi:10.5281/zenodo.1252036
- Bahramian, A., Strader, J., Chomiuk, L., et al. 2018, *ApJ*, **864**, 28
- Barlow, E. J., Knigge, C., Bird, A. J., et al. 2006, *MNRAS*, **372**, 224
- Bassa, C., Pooley, D., Homer, L., et al. 2004, *ApJ*, **609**, 755
- Bassa, C. G., Patruno, A., Hessels, J. W. T., et al. 2014, *MNRAS*, **441**, 1825
- Bassa, C. G., Pooley, D., Verbunt, F., et al. 2008, *A&A*, **488**, 921
- Baumgardt, H., & Hilker, M. 2018, *MNRAS*, **478**, 1520
- Baumgartner, W. H., Tueller, J., Markwardt, C. B., et al. 2013, *ApJS*, **207**, 19
- Belczyński, K., Mikołajewska, J., Munari, U., Ivison, R. J., & Friedjung, M. 2000, *A&AS*, **146**, 407
- Belloni, D., Giersz, M., Rivera Sandoval, L. E., Askar, A., & Ciecieląg, P. 2019, *MNRAS*, **483**, 315
- Belloni, D., Mikołajewska, J., Ilkiewicz, K., et al. 2020, *MNRAS*, **496**, 3436
- Bhattacharya, S., Heinke, C. O., Chugunov, A. I., et al. 2017, *MNRAS*, **472**, 3706
- Bogdanov, S., Deller, A. T., Miller-Jones, J. C. A., et al. 2018, *ApJ*, **856**, 54
- Bogdanov, S., van den Berg, M., Servillat, M., et al. 2010, *ApJ*, **730**, 81
- Bozzo, E., Ferrigno, C., Stevens, J., et al. 2011, *A&A*, **535**, L1
- Broos, P. S., Townsley, L. K., Feigelson, E. D., et al. 2010, *ApJ*, **714**, 1582
- Buchner, J., Georgakakis, A., Nandra, K., et al. 2014, *A&A*, **564**, A125
- Cackett, E. M., Wijnands, R., Heinke, C. O., et al. 2006, *MNRAS*, **369**, 407
- Cadelano, M., Ransom, S. M., Freire, P. C. C., et al. 2018, *ApJ*, **855**, 125
- Cash, W. 1979, *ApJ*, **228**, 939
- Cheng, Z., Li, Z., Fang, T., Li, X., & Xu, X. 2019a, *ApJ*, **883**, 90
- Cheng, Z., Li, Z., Li, X., Xu, X., & Fang, T. 2019b, *ApJ*, **876**, 59
- Cheng, Z., Li, Z., Xu, X., et al. 2018, *ApJ*, **869**, 52
- Chomiuk, L., Strader, J., Maccarone, T. J., et al. 2013, *ApJ*, **777**, 69
- Clark, G. W. 1975, *ApJL*, **199**, L143
- Cohn, H. N., Lugger, P. M., Couch, S., et al. 2010, *ApJ*, **722**, 20
- Corbel, S., Coriat, M., Brocksopp, C., et al. 2013, *MNRAS*, **428**, 2500
- Dai, S., Johnston, S., Kerr, M., et al. 2020, *ApJL*, **888**, L18
- Damiani, F., Maggio, A., Micela, G., & Sciortino, S. 1997, *ApJ*, **483**, 370
- Davies, M. B. 1997, *MNRAS*, **288**, 117
- Davis, J. E. 2001, *ApJ*, **562**, 575
- de Martino, D., Belloni, T., Falanga, M., et al. 2013, *A&A*, **550**, A89
- de Martino, D., Falanga, M., Bonnet-Bidaud, J.-M., et al. 2010, *A&A*, **515**, A25
- Degenaar, N., Brown, E. F., & Wijnands, R. 2011, *MNRAS*, **418**, L152
- Degenaar, N., & Wijnands, R. 2009, *A&A*, **495**, 547
- Degenaar, N., Wijnands, R., Bahramian, A., et al. 2015, *MNRAS*, **451**, 2071
- Deller, A. T., Moldon, J., Miller-Jones, J. C. A., et al. 2015, *ApJ*, **809**, 13
- Dobrotka, A., Lasota, J., & Menou, K. 2006, *ApJ*, **640**, 288
- Edmonds, P. D., Gilliland, R. L., Heinke, C. O., & Grindlay, J. E. 2003, *ApJ*, **596**, 1197
- Edmonds, P. D., Kahabka, P., & Heinke, C. O. 2004, *ApJ*, **611**, 413
- Fabian, A. C., Pringle, J. E., & Rees, M. J. 1975, *MNRAS*, **172**, 15P
- Feigelson, E. D., & Babu, G. J. 2012, *Modern Statistical Methods for Astronomy* (Cambridge: Cambridge Univ. Press)
- Fender, R. P., Gallo, E., & Jonker, P. G. 2003, *MNRAS*, **343**, L99
- Feroz, F., Hobson, M. P., Cameron, E., & Pettitt, A. N. 2019, *OJAp*, **2**, 10
- Foight, D. R., Güver, T., Özel, F., & Slane, P. O. 2016, *ApJ*, **826**, 66
- Foreman-Mackey, D. 2016, *JOSS*, **1**, 24
- Forestell, L. M., Heinke, C. O., Cohn, H. N., et al. 2014, *MNRAS*, **441**, 757
- Freire, P. C. C., Ridolfi, A., Kramer, M., et al. 2017, *MNRAS*, **471**, 857
- Fruscione, A., McDowell, J. C., Allen, G. E., et al. 2006, *Proc. SPIE*, **6270**, 62701V
- Gallo, E., Degenaar, N., & van den Eijnden, J. 2018, *MNRAS*, **478**, L132
- Gallo, E., Miller, B. P., & Fender, R. 2012, *MNRAS*, **423**, 590
- Gallo, E., Miller-Jones, J. C. A., Russell, D. M., et al. 2014, *MNRAS*, **445**, 290
- Galloway, D. K., Muno, M. P., Hartman, J. M., Psaltis, D., & Chakrabarty, D. 2008, *ApJS*, **179**, 360
- Gibaud, L., Bazzano, A., Bozzo, E., et al. 2011, *ATel*, **3565**, 1
- Giesers, B., Dreizler, S., Husser, T.-O., et al. 2018, *MNRAS*, **475**, L15
- Giesers, B., Kamann, S., Dreizler, S., et al. 2019, *A&A*, **632**, A3
- Gliese, W., & Jahreiß, H. 1991, Preliminary Version of the Third Catalogue of Nearby Stars, On: The Astronomical Data Center CD-ROM: Selected Astronomical Catalogs (Greenbelt, MD; Goddard Space Flight Center)
- Grindlay, J. E. 1993, in ASP Conf. Ser. 48: The Globular Cluster-Galaxy Connection, ed. G. H. Smith & J. P. Brodie (San Francisco, CA: ASP), **156**
- Grindlay, J. E., Cool, A. M., Callanan, P. J., et al. 1995, *ApJL*, **455**, L47
- Grindlay, J. E., Heinke, C., Edmonds, P. D., & Murray, S. S. 2001, *Sci*, **292**, 2290
- Guillot, S., Rutledge, R. E., Brown, E. F., Pavlov, G. G., & Zavlin, V. E. 2009, *ApJ*, **699**, 1418
- Guillot, S., Servillat, M., Webb, N. A., & Rutledge, R. E. 2013, *ApJ*, **772**, 7
- Gusinskaia, N. V., Russell, T. D., Hessels, J. W. T., et al. 2020, *MNRAS*, **492**, 1091
- Haggard, D., Cool, A. M., & Davies, M. B. 2009, *ApJ*, **697**, 224
- Harris, W. E. 1996, *AJ*, **112**, 1487
- Heinke, C. O., Cohn, H. N., & Lugger, P. M. 2009, *ApJ*, **692**, 584
- Heinke, C. O., Grindlay, J. E., & Edmonds, P. D. 2005a, *ApJ*, **622**, 556
- Heinke, C. O., Grindlay, J. E., Edmonds, P. D., et al. 2005b, *ApJ*, **625**, 796
- Heinke, C. O., Grindlay, J. E., Lloyd, D. A., & Edmonds, P. D. 2003a, *ApJ*, **588**, 452
- Heinke, C. O., Grindlay, J. E., Lugger, P. M., et al. 2003b, *ApJ*, **598**, 501
- Heinke, C. O., Ivanov, M. G., Koch, E. W., et al. 2020, *MNRAS*, **492**, 5684
- Heinke, C. O., Rybicki, G. B., Narayan, R., & Grindlay, J. E. 2006a, *ApJ*, **644**, 1090
- Heinke, C. O., Wijnands, R., Cohn, H. N., et al. 2006b, *ApJ*, **651**, 1098
- Henleywillis, S., Cool, A. M., Haggard, D., et al. 2018, *MNRAS*, **479**, 2834
- Hessels, J. W. T., Ransom, S. M., Stairs, I. H., Kaspi, V. M., & Freire, P. C. C. 2007, *ApJ*, **670**, 363
- Hills, J. G. 1976, *MNRAS*, **175**, 1P
- Homan, J., & Pooley, D. 2012, *ATel*, **4302**, 1
- Hong, J., Vesperini, E., Belloni, D., & Giersz, M. 2017, *MNRAS*, **464**, 2511
- Hui, C. Y., Cheng, K. S., Wang, Y., et al. 2011, *ApJ*, **726**, 100
- Hunter, J. D. 2007, *CSE*, **9**, 90
- Hynes, R. I., Torres, M. A. P., Heinke, C. O., et al. 2014, *ApJ*, **780**, 11
- Ivanova, N., Heinke, C. O., Rasio, F. A., et al. 2006, *MNRAS*, **372**, 1043
- Jaodand, A., Archibald, A. M., Hessels, J. W. T., et al. 2016, *ApJ*, **830**, 122
- Joye, W. A., & Mandel, E. 2003, in ASP Conf. Ser. 295, New Features of SAOImage DS9, ed. H. E. Payne, R. I. Jedrzejewski, & R. N. Hook (San Francisco, CA: ASP), **489**
- Kenyon, S. J., & Garcia, M. R. 2016, *AJ*, **152**, 1
- Kluyver, T., Ragan-Kelley, B., Pérez, F., et al. 2016, in Positioning and Power in Academic Publishing: Players, Agents and Agendas, ed. F. Loizides & B. Schmidt (Amsterdam: IOS Press), 87
- Kolmogorov, A. 1933, *Inst. Ital. Attuari. Giorn*, **4**, 83
- Kulkarni, S. R., Hut, P., & McMillan, S. 1993, *Natur*, **364**, 421
- Kundu, A., Maccarone, T. J., & Zepf, S. E. 2007, *ApJ*, **662**, 525
- Kundu, A., & Zepf, S. E. 2007, *ApJL*, **660**, L109
- Linares, M. 2014, *ApJ*, **795**, 72
- Linares, M., Bahramian, A., Heinke, C., et al. 2014, *MNRAS*, **438**, 251
- Lü, G., Yungelson, L., & Han, Z. 2006, *MNRAS*, **372**, 1389
- Lugger, P. M., Cohn, H. N., Cool, A. M., Heinke, C. O., & Anderson, J. 2017, *ApJ*, **841**, 53
- Lugger, P. M., Cohn, H. N., Heinke, C. O., Grindlay, J. E., & Edmonds, P. D. 2007, *ApJ*, **657**, 286
- Lyne, A. G., Brinklow, A., Middleditch, J., Kulkarni, S. R., & Backer, D. C. 1987, *Natur*, **328**, 399
- Lyne, A. G., Mankelov, S. H., Bell, J. F., & Manchester, R. N. 2000, *MNRAS*, **316**, 491
- Maccarone, T. J., Kundu, A., Zepf, S. E., & Rhode, K. L. 2007, *Natur*, **445**, 183
- Marsh, T. R., Gänsicke, B. T., Hümmerich, S., et al. 2016, *Natur*, **537**, 374
- Mateos, S., Warwick, R. S., Carrera, F. J., et al. 2008, *A&A*, **492**, 51
- Mattu, A. 2014, HEASoft: Unified Release of FTOOLS and XANADU, Astrophysics Source Code Library, ascl:1408.004
- Maxwell, J. E., Lugger, P. M., Cohn, H. N., et al. 2012, *ApJ*, **756**, 147
- McClintock, J. E., Narayan, R., & Rybicki, G. B. 2004, *ApJ*, **615**, 402
- Migliari, S., & Fender, R. P. 2006, *MNRAS*, **366**, 79
- Miller, J. M., Maitra, D., Cackett, E. M., Bhattacharyya, S., & Strohmayer, T. E. 2011, *ApJL*, **731**, L7
- Miller-Jones, J. C. A., Strader, J., Heinke, C. O., et al. 2015, *MNRAS*, **453**, 3918
- Morscher, M., Pattabiraman, B., Rodriguez, C., Rasio, F. A., & Umbreit, S. 2015, *ApJ*, **800**, 9
- Morscher, M., Umbreit, S., Farr, W. M., & Rasio, F. A. 2013, *ApJL*, **763**, L15
- Mukai, K., Luna, G. J. M., Cusumano, G., et al. 2016, *MNRAS*, **461**, L1
- Munari, U. 2019, arXiv:1909.01389
- Munari, U., & Renzini, A. 1992, *ApJL*, **397**, L87
- Oliphant, T. E. 2006, *A Guide to NumPy*, Vol. 1 (USA: Trelgol Publishing)
- Ootes, L. S., Vats, S., Page, D., et al. 2019, *MNRAS*, **487**, 1447

- Papitto, A., Ferrigno, C., Bozzo, E., et al. 2013, *Natur*, 501, 517
- Patterson, J. 1994, *PASP*, 106, 209
- Patterson, J., & Raymond, J. C. 1985, *ApJ*, 292, 535
- Perez, F., & Granger, B. E. 2007, *CSE*, 9, 21
- Picard, A., & Johnston, H. M. 1995, *A&AS*, 112, 89
- Pietrukowicz, P., Mróz, P., Udalski, A., Soszyński, I., & Skowron, J. 2019, *ApJL*, 881, L41
- Plotkin, R. M., Miller-Jones, J. C. A., Gallo, E., et al. 2017, *ApJ*, 834, 104
- Pooley, D., Homan, J., Heinke, C. O., et al. 2011, *ATel*, 3627, 1
- Pooley, D., Lewin, W. H. G., Anderson, S. F., et al. 2003, *ApJL*, 591, L131
- Pooley, D., Lewin, W. H. G., Homer, L., et al. 2002, *ApJ*, 569, 405
- Pretorius, M. L., & Mukai, K. 2014, *MNRAS*, 442, 2580
- Ransom, S. M., Hessels, J. W. T., Stairs, I. H., et al. 2005, *Sci*, 307, 892
- Ridolfi, A., Freire, P. C. C., Torne, P., et al. 2016, *MNRAS*, 462, 2918
- Rivera Sandoval, L. E., van den Berg, M., Heinke, C. O., et al. 2018a, *MNRAS*, 475, 4841
- Rivera Sandoval, L. E., Wijnands, R., Degenaar, N., et al. 2018b, *MNRAS*, 479, 2777
- Rodríguez, C. L., Haster, C.-J., Chatterjee, S., Kalogera, V., & Rasio, F. A. 2016, *ApJL*, 824, L8
- Russell, T. D., Degenaar, N., Wijnands, R., et al. 2018, *ApJL*, 869, L16
- Russell, T. D., Miller-Jones, J. C. A., Sivakoff, G. R., et al. 2016, *MNRAS*, 460, 3720
- Rutledge, R. E., Bildsten, L., Brown, E. F., Pavlov, G. G., & Zavlin, V. E. 2002, *ApJ*, 578, 405
- Sarajedini, A., Bedin, L. R., Chaboyer, B., et al. 2007, *AJ*, 133, 1658
- Sarazin, C. L., Kundu, A., Irwin, J. A., et al. 2003, *ApJ*, 595, 743
- Schwöpe, A. D. 2018, *A&A*, 619, A62
- Servillat, M., Webb, N. A., & Barret, D. 2008, *A&A*, 480, 397
- Shara, M. M., & Hurley, J. R. 2006, *ApJ*, 646, 464
- Shaw, A. W., Heinke, C. O., Maccarone, T. J., et al. 2020, *MNRAS*, 492, 4344
- Shishkovsky, L., Strader, J., Chomiuk, L., et al. 2018, *ApJ*, 855, 55
- Sigurdsson, S., & Hernquist, L. 1993, *Natur*, 364, 423
- Smirnov, N. 1948, *Ann. Math. Statist.*, 19, 279
- Stacey, W. S., Heinke, C. O., Cohn, H. N., Lugger, P. M., & Bahramian, A. 2012, *ApJ*, 751, 62
- Steiner, A. W., Heinke, C. O., Bogdanov, S., et al. 2018, *MNRAS*, 476, 421
- Strader, J., Chomiuk, L., Maccarone, T. J., Miller-Jones, J. C. A., & Seth, A. C. 2012, *Natur*, 490, 71
- Suleimanov, V. F., Doroshenko, V., & Werner, K. 2019, *MNRAS*, 482, 3622
- Sutantyo, W. 1975, *A&A*, 44, 227
- Tetarenko, B. E., Sivakoff, G. R., Heinke, C. O., & Gladstone, J. C. 2016, *ApJS*, 222, 15
- Tremou, E., Strader, J., Chomiuk, L., et al. 2018, *ApJ*, 862, 16
- Tudor, V., Miller-Jones, J. C. A., Patruno, A., et al. 2017, *MNRAS*, 470, 324
- van den Berg, M., Grindlay, J., Laycock, S., et al. 2006, *ApJL*, 647, L135
- van der Walt, S., Colbert, S. C., & Varoquaux, G. 2011, *CSE*, 13, 22
- Verbunt, F. 2001, *A&A*, 368, 137
- Verbunt, F., Bunk, W., Hasinger, G., & Johnston, H. M. 1995, *A&A*, 300, 732
- Verbunt, F., & Hut, P. 1987, in *IAU Symp. 125: The Origin and Evolution of Neutron Stars*, ed. D. J. Helfand & J.-H. Huang (Dordrecht: Reidel), 187
- Verbunt, F., & Lewin, W. H. G. 2006, in *Globular Cluster X-ray Sources (In: Compact Stellar X-ray Sources)*, ed. W. H. G. Lewin & M. van der Klis (Cambridge: Cambridge Univ. Press), 341
- Verner, D. A., Ferland, G. J., Korista, K. T., & Yakovlev, D. G. 1996, *ApJ*, 465, 487
- Virtanen, P., Gommers, R., Oliphant, T. E., et al. 2020, *NatMe*, 17, 261
- Walter, F. M., & Bowyer, S. 1981, *ApJ*, 245, 671
- Weisskopf, M. C., Wu, K., Trimble, V., et al. 2007, *ApJ*, 657, 1026
- Wenger, M., Ochsenein, F., Egret, D., et al. 2000, *A&AS*, 143, 9
- Wijnands, R., Heinke, C. O., & Grindlay, J. E. 2002, *ApJ*, 572, 1002
- Wijnands, R., Heinke, C. O., Pooley, D., et al. 2005, *ApJ*, 618, 883
- Wijnands, R., in't Zand, J. J. M., Rupen, M., et al. 2006, *A&A*, 449, 1117
- Wijnands, R., & van der Klis, M. 1998, *Natur*, 394, 344
- Wijnands, R., Yang, Y. J., Degenaar, N., et al. 2011, *ATel*, 3595, 1
- Wilms, J., Allen, A., & McCray, R. 2000, *ApJ*, 542, 914